Changes in ENSO oscillatory dynamics associated with zonal shifts in air-sea coupling region

Brandon A. Molina,[a] Pedro N. DiNezio,[a] and Clara Deser[b]

[a] *Atmospheric and Oceanic Sciences Department, University of Colorado, Boulder, Colorado*

[b] *National Center for Atmospheric Research, Boulder, Colorado*

Corresponding author: Brandon A. Molina, brandon.molina@colorado.edu

ABSTRACT: El Niño–Southern Oscillation (ENSO) oscillates between warm (El Niño) and cold (La Niña) phases, but observations indicate that this oscillatory behavior is irregular and asymmetric. Using the NCAR Community Earth System Model 1 (CESM), we investigate how the oscillatory dynamics of ENSO change across different climatic states. Our simulations of two glacial climates (Last Glacial Maximum, 21 ka; deglacial state, 15 ka), a pre-industrial baseline (piControl), and two greenhouse warming scenarios ($2xCO_2$; $4xCO_2$) reveal distinct dynamical regimes of oscillatory behavior driven by zonal shifts in air-sea coupling. Under pre-industrial conditions, maximum wind-sea-surface temperature coupling occurs near the Niño-3.4 region and CESM reproduces the observed asymmetry of ENSO oscillatory behavior; El Niño events often rapidly decay into La Niña, while La Niña events rarely lead to El Niño but rather decay slowly back to neutral conditions. In simulated glacial climates, ENSO is non-oscillatory because the air-sea coupling region shifts westward of the Niño-3.4 region. In the western Pacific, a deeper thermocline weakens the delayed positive feedback needed for events to grow into the opposite phase, causing both El Niño and La Niña to decay back to neutral conditions. Conversely, in warmer climates, ENSO becomes more oscillatory and symmetric as the air-sea coupling region shifts eastward of the Niño3.4 region. In the eastern Pacific, a shallower thermocline strengthens its positive feedback, enabling more frequent and consistent transitions between phases. This sensitivity of ENSO oscillatory behavior to the longitude of maximum air-sea coupling suggests that future changes to ENSO predictability in response to external forcings could be significant.

1. Introduction

El Niño-Southern Oscillation (ENSO) is often considered as a quasi-regular oscillation between El Niño and La Niña. However, the short observational record reveals a crucial asymmetry—while most El Niño events reliably transition into La Niña the reverse rarely happens (Kessler 2002; Okumura and Deser 2010). This asymmetry poses a challenge to understanding ENSO as a simple cycle, prompting a more detailed description of its behavior. We use the terms "oscillatory behavior" and "oscillatory dynamics" in this study to refer to the consistency of phase transitions, the temporal evolution of events, and the primary periodicity of the phenomenon. This observed asymmetry has posed a challenge for simpler conceptual models of ENSO, such as the delayed oscillator paradigm (Suarez and Schopf 1988; Jin 1997), which, while foundational for understanding core dynamics involving thermocline feedbacks, often depict a more regular, symmetric oscillation. These models typically struggle to fully capture the irregularity and transition asymmetries inherent in the observed ENSO cycle (Timmermann et al. 2018; Capotondi et al. 2015), though Eastern Pacific (EP) and Central Pacific (CP) event diversity has been established in intermediate-complexity models (Takahashi et al. 2011). While the mechanisms for the onset, persistence, and decay of La Niña are well understood (Okumura et al. 2011; DiNezio and Deser 2014; Seager et al. 2021), how the oscillatory dynamics of both El Niño and La Niña might change under altered climate conditions remains largely unexplored. This is a critical question, as the lack of a consistent La Niña-to-El Niño transition is a major reason for the limited predictability of El Niño events (Planton et al. 2018; Dommenget et al. 2012).

Among General Circulation Models (GCMs), the Community Earth System Model (CESM) is one of the most realistic simulators of ENSO's temporal evolution, capturing the observed irregularity and asymmetries in event duration and transitions that are often missing in more regular, overly oscillatory models (Deser et al. 2012; DiNezio et al. 2017a). These improvements stem from a more realistic simulation of zonal wind anomalies and their meridional structure (Capotondi et al. 2020), which better excites upper-ocean adjustments to wind stress curl (Choi et al. 2013; DiNezio and Deser 2014). Such advances in simulating fundamental ENSO dynamics provide a robust foundation for examining how oscillatory behavior shifts under altered climate states.

Evidence from paleoclimate records and simulations in models suggest that ENSO variability can change in response to a new mean state—from the Last Glacial Maximum (LGM) to future greenhouse gas simulations. During the last deglaciation period, ENSO behavior has varied in response to orbital forcing, rising greenhouse gases, and retreating ice sheets (Liu et al. 2014). While proxy records of variations in ENSO strength during this period are still debated (Zhu et al. 2017; Tudhope et al. 2001; Cane 2005), modeling efforts indicate a modest rise in variability throughout the deglaciation (Liu et al. 2014; Thirumalai et al. 2024) with potentially strong sensitivities to individual forcings; for example, orbital precession drove changes in the seasonal cycle of the cold tongue, while ice sheet retreat altered tropical atmospheric circulation (Liu et al. 2014). In particular, ENSO has been simulated to have a strong sensitivity to orbital forcing during the mid-Holocene, which modulated the seasonal cycle and ENSO amplitude (Clement et al. 2001), and to the retreat of the North American ice sheet around 14 ka, which altered atmospheric circulation and reorganized the tropical Pacific (Liu et al. 2014; Löfverström and Lora 2017). The sensitivity of ENSO to these past forcings highlights the importance of investigating how its characteristics might change in a warming world. Our experimental framework (Table 1) accounts for these varying climate states by incorporating appropriate boundary conditions—such as orbital and ice-sheet forcings—beyond CO_2 alone (see Thirumalai et al. (2024)). As shown in Fig. 1, these forcings successfully produce a broad spectrum of mean states, ranging from the enhanced equatorial warming and weakened zonal gradients of greenhouse climates to the characteristic cooling patterns of glacial simulations. This wide range of simulated states is particularly relevant because, while many models predict a weakening Walker circulation over the 21st century (Seager et al. 2019; Vecchi et al. 2006), the specific ENSO response to such warming is highly model-dependent (Maher et al. 2021). For example, multi-model projections show an increase in the occurrence of multiyear La Niña under greenhouse warming (Geng et al. 2023; Wang et al. 2023), yet it remains unclear how this would affect the onset of a subsequent El Niño. While several studies have examined changes in ENSO transitions under warming (Freund et al. 2024), few have specifically investigated the mechanisms controlling the consistency of phase transitions across a wide range of mean states, from glacial conditions to extreme greenhouse warming. Our study addresses this gap by identifying the longitudinal location of the air-sea coupling region as a key control on oscillatory dynamics.

To address the uncertainties of past and future ENSO oscillatory behavior, it is crucial to focus on the specific physical processes that can change under altered conditions. The delayed thermocline feedback governing ENSO event transitions (Suarez and Schopf 1988; Jin 1997) involves multiple physical processes that can change under different climate states, such as the coupling between surface winds, thermocline depth, and sea-surface temperature (SST) variations (Timmermann et al. 2018; Capotondi et al. 2015). For instance, changes in the zonal extent of the western Pacific warm pool can affect how winds respond to SST variations by modulating the area along the equatorial Pacific favoring atmospheric convection (Picaut et al. 1996). Conversely, changes in upper ocean stratification can also affect how the thermocline responds to wind variability, but also the influence of thermocline variability on SST variations (Yeh et al. 2010). Understanding how these specific processes are modified under climates ranging from past glacial conditions to future greenhouse warming scenarios, we can gain a clearer understanding of the mechanisms that control ENSO's oscillatory behavior and improve predictions of its future.

Here we examine the mechanisms driving changes in ENSO's oscillatory dynamics using a set of five simulations performed with CESM1 that span a wide range of past and future climate conditions. We used four simulated climates and a pre-industrial control run to investigate ENSO changes. Two of these simulations represent past climates with lower greenhouse gas concentrations and global surface temperatures than today: 21,000 years ago (21 ka) and 15,000 years ago (15 ka). The other two simulations represent future climates with higher global temperatures due to double ($2xCO_2$) and quadruple ($4xCO_2$) the pre-industrial CO_2 concentration. A long pre-industrial simulation serves as a control to evaluate the statistical significance of ENSO changes. We first describe the changes in the mean state and its effects on the magnitude and spatial expression of ENSO variability for SST and zonal wind stress anomalies in the tropical Pacific. We found the zonal shifts in simulated patterns of co-variability between SST and zonal wind stress anomalies, motivating us to define a climate-specific center of action. This preferred coupling region is defined in each climate state as the location where SSTs and wind are most tightly correlated. We then describe how this climate-specific coupling region shifts zonally in response to mean state changes, which in turn lead to distinct changes in oscillatory behavior. Finally, we use a heat budget analysis to diagnose the specific feedbacks responsible for these changes, providing

a comprehensive physical explanation for how the location of the air-sea coupling region governs ENSO's oscillatory regime.

2. Data and Methods

We analyzed output generated using the Community Earth System Model Version 1.2 (CESM1) – a coupled general circulation model consisting of the atmosphere, ocean, land, and cryosphere components, linked through a flux coupler (Hurrell et al. 2013). The CESM1 retains advances in the simulation of ENSO from its predecessor, CCSM4, with both versions simulating the observed asymmetries in the evolution of El Niño and La Niña events with high realism (Deser et al. 2012; DiNezio et al. 2017a). The atmospheric component is the Community Atmosphere Model Version 5 (CAM5), including new schemes for the simulation of moist turbulence, a shallow convection, cloud microphysics, and aerosol-cloud-rainfall interactions (Hurrell et al. 2013). In our simulations, CAM5 was configured on a finite volume grid at a nominal horizontal resolution of 2° with 30 pressure levels for the vertical coordinate. The land component is the Community Land Model Version 4 (CLM4) configured on the same horizontal grid as the atmosphere model. The ocean model is the Parallel Ocean Program Version 2 (POP2) configured at the nominal horizontal resolution of 1° with increased meridional resolution of about 1/3°approaching the equatorial wave guide, and 60 vertical levels. POP2 has parameterizations that simulate overflows, tidal mixing, and eddy mixing.

Our simulations span a range of externally forced changes in the mean climate state and variability in the tropical Pacific. Two simulations represent climate conditions under glacial conditions, one for the Last Glacial Maximum (LGM) 21,000 years before present (21 ka BP LGM) and the other for an interval during the last deglaciation 15,000 year before present (15 ka BP deglacial). These simulations were run with realistic ice sheets topography, coastlines, greenhouse concentrations, and insolation patterns following paleoclimate modeling protocols as described in Thirumalai et al. (2024). The 21 ka BP climate has orbital forcing closest to our current climate while the 15 ka BP deglacial has orbital forcing of precession that is substantially different from today leading to altered insolation affecting the annual cycle of the cold tongue – a well known driver of ENSO changes (Clement et al. 1999; Timmermann et al. 2007). Two additional simulations represent warmer climates under doubled and quadrupled atmospheric CO_2 concentrations relative to PI

TABLE 1: Boundary conditions of the simulated climates by CESM1.

Simulation	Atmospheric CO_2 (ppm)	Simulation Length (Yrs)
4xCO_2	1120	300
2xCO_2	560	500
PI	280	1500
15 ka BP	230	500
21 ka BP	190	500

values (2xCO_2 and 4xCO_2). All four simulations were run until global mean surface temperature reached equilibrium. The analysis was performed on subsequent output from an equilibrated climate. We use 500 years of monthly output for the analysis, except for the 4xCO_2 simulation for which we use the last 300 years of near equilibrated climate (Table 1). All four simulations have a drift in global mean surface temperature less than 0.11 K per century during the analysis interval (Thirumalai et al. 2024). We compare variability in these simulations relative to a control simulation of PI climate. The length of this simulation, 1500 years, allows us to quantify unforced centennial variability under constant PI forcing. This was essential to assess whether the changes simulated under glacial and greenhouse conditions are forced. Note that our glacial and greenhouse warming simulations have a length well within the requirement to identify externally forced changes in ENSO in multi-century simulations (Wittenberg 2009). The 4xCO_2 simulation shows a very regular ENSO with reduced centennial variability allowing the use of only 300 years to detect changes relative to the PI control.

We used ocean and atmosphere variables from the CESM1 standard output to analyze ENSO dynamics and quantify physical processes. To capture the seasonal modulation of ENSO variability, all variables were analyzed at monthly temporal resolution. Anomalies were then calculated by removing the long-term monthly mean seasonal cycle from each year of the simulations. Finally, to isolate and focus on ENSO variability, monthly anomalies were smoothed with a bandpass filter spanning 6 months to 10 years. In addition to the standard CESM1 output, we also calculated the depth of the thermocline, defined as the depth at which the vertical temperature gradient is maximized, from 3-dimensional ocean model output. This calculation was restricted to the latitude band between 5°N and 5°S to represent the equatorial region. Unlike the typical definition based on

the 20°C isotherm, using the depth of the maximum temperature gradient identifies the depth of the thermocline regardless of changes in ocean temperatures in each climate state (Vecchi and Soden 2007; DiNezio et al. 2009; Yang and Wang 2009). We also calculate the eastern edge of the western Pacific warm pool as the zero-contour of the atmospheric vertical velocity in pressure coordinates, ω, at the 500 hPa level, using the same latitude band (5°N–5°S). Unlike the definition based on the 28°C SST contour (De Deckker 2016), our definition of the warm pool edge is independent of the changes in SST in each climate state as it captures regions more prone to experience atmospheric convection. Locating the warm pool edge along the equatorial Pacific is important to identify the region where atmospheric convection will be most sensitive to changes in SST associated with ENSO.

To evaluate the realism of El Niño and La Niña transitions in our PI control simulation, we analyze observational SST and surface wind stress data. For SST, we use the NOAA Extended Reconstructed Sea Surface Temperature Version 5 (ERSSTv5) dataset (Huang et al. 2017), which spans 1854–2023 and provides a robust basis for estimating ENSO statistics and comparing them with our PI control simulation. Historical forcings have shown limited influence on ENSO variability (Maher et al. 2023), enabling meaningful comparisons between PI simulations and historical data. Surface wind stress data are drawn from the fifth-generation ECMWF atmospheric reanalysis (ERA5) (Hersbach et al. 2020). To account for long-term trends, both observational datasets have been quadratically detrended. By using SST and surface wind stress data from the common period of 1950–2023, we identify the coupling region under current climate conditions and assess the methodology for locating this region in the PI control simulation.

Definition of ENSO events

We define ENSO events using a novel Climate-Specific Niño (CSN) index that accounts for the shifting dynamics of the coupling region – the area with strongest air-sea interactions along the equatorial Pacific – across different climate states. Unlike the conventional Niño3.4 region, we use an adjusted region with zonally varying boundaries. The specific longitudinal bounds are detailed in Table 2, and the methodology for determining these adjustments is explained in Results section 2. To mitigate biases arising from varying ENSO amplitudes, we implement a standardized method for detecting El Niño and La Niña. We identify these events events when the CSN SST

Table 2: Coupling region to compute ENSO variability.

Simulation	Longitude Bounds
4xCO_2	145°W - 95°W
2xCO_2	150°W - 100°W
PI	170°W - 120°W
15 ka BP	145°E - 165°W
21 ka BP	165°E - 145°W

anomalies during the December-January-February (DJF) season exceed +1 or -1 standard deviation, respectively. This normalization technique ensures a consistent and unbiased detection of ENSO events across diverse climatic conditions. To provide a comprehensive understanding of ENSO's temporal evolution, we employ a systematic composite analysis methodology. By aligning the Decembers of all single-year and final year of multi-year events, we can focus on the transitions out of each ENSO phase. This methodology allows us to systematically track the evolution of ENSO events before, during, and after their peak, revealing the underlying mechanisms driving their initiation, growth, and decay. This approach provides a robust framework for analyzing El Niño and La Niña transitions across different climate states, ensuring consistent event detection and allowing us to explore the processes governing ENSO phase transitions.

Mixed Layer Heat Budget

We perform an upper ocean heat budget analysis following DiNezio and Deser (2014) in order to diagnose the physical processes involved in the transitions between El Niño and La Niña.

$$\rho_0 c_p H \frac{\partial [T']}{\partial t} = -\rho_0 c_p \int_{-H}^{0} \left(u' \frac{\partial \overline{T}}{\partial x} + w' \frac{\partial \overline{T}}{\partial z} + \overline{w} \frac{\partial T'}{\partial z} \right) \mathrm{d}z + Q'_{atm} + \epsilon \qquad (1)$$

The heat budget equation (1) is computed as a balance between the heat storage rate within the upper ocean mixed layer (left hand side of equation 1) and the advective heat fluxes into the same layer as well as the net atmospheric heat flux (right hand side of equation 1). H represents the depth of the layer in the upper ocean over which the heat budget is computed. Our choice of H ensures that the anomalies of temperature averaged over the surface layer, $[T']$, effectively capture the magnitude of evolution of SST anomalies. Our approach to closing the heat budget for $[T']$

focuses on the three main thermal advection terms involved in ENSO dynamics: (1) anomalous horizontal advection of the mean temperature gradient ($\frac{\partial \overline{T}}{\partial x}$) by the anomalous zonal velocity (u'), $-u'\frac{\partial \overline{T}}{\partial x}$, a term associated with zonal ocean current variations; (2) anomalous vertical advection of mean temperature gradient ($\frac{\partial \overline{T}}{\partial z}$) by the anomalous vertical velocity (w'), $-w'\frac{\partial \overline{T}}{\partial z}$, a term associated with upwelling variations; and (3) anomalous vertical advection of anomalous temperature gradient ($\frac{\partial T'}{\partial z}$) by the mean vertical velocity ($\overline{w}$), $-\overline{w}\frac{\partial T'}{\partial z}$, a term associated with thermocline depth variations. In the results, we demonstrate how these three terms plus the anomalous net air-sea heat flux balance the $[T']$ temporal tendency. This allows us to use a composite heat budget for El Niño events to diagnose the processes explaining the oscillatory dynamics.

3. Results

a. Changes in the Pacific mean state and variability

Our simulations show a wide range of changes in the mean climate of the equatorial Pacific relative to the PI simulation that could affect the physical processes governing ENSO dynamics. The simulations of glacial climates, 21 ka BP and 15 ka BP, exhibit a pattern of enhanced equatorial cooling in the tropical Pacific, which we emphasize by removing the tropical mean SST changes (Fig.1a & 1b, shading). This pattern of cooling intensifies towards the eastern Pacific leading to a stronger zonal SST gradient along the equator together with stronger southeasterly trade winds and surface wind divergence along the equator (Fig. 1a-b, vectors). Conversely, the simulations under increased greenhouse forcing, $2xCO_2$ and $4xCO_2$, exhibit a pattern of enhanced equatorial warming that intensifies towards the eastern Pacific leading to a weaker zonal SST gradient along the equator (Fig. 1c-d, shading) and weaker southeasterly trade winds and surface wind divergence (Fig. 1c-d, vectors). These patterns of cooling and warming are part of well-known climate responses simulated by CMIP-class models in response to greenhouse forcing (Vecchi and Soden 2007; DiNezio et al. 2009; Li et al. 2016). In models, these responses arise as part of a coupled response to changes in the global Walker circulation, which weakens in response to warming and strengthens in response to cooling (Vecchi and Soden 2007; DiNezio et al. 2011). The associated changes in the winds in the equatorial Pacific drive characteristic ocean responses, mainly changes in upwelling and thermocline depth, that amplify the temperature response along the equator (DiNezio et al. 2009). The changes simulated across all climates are highly consistent with this

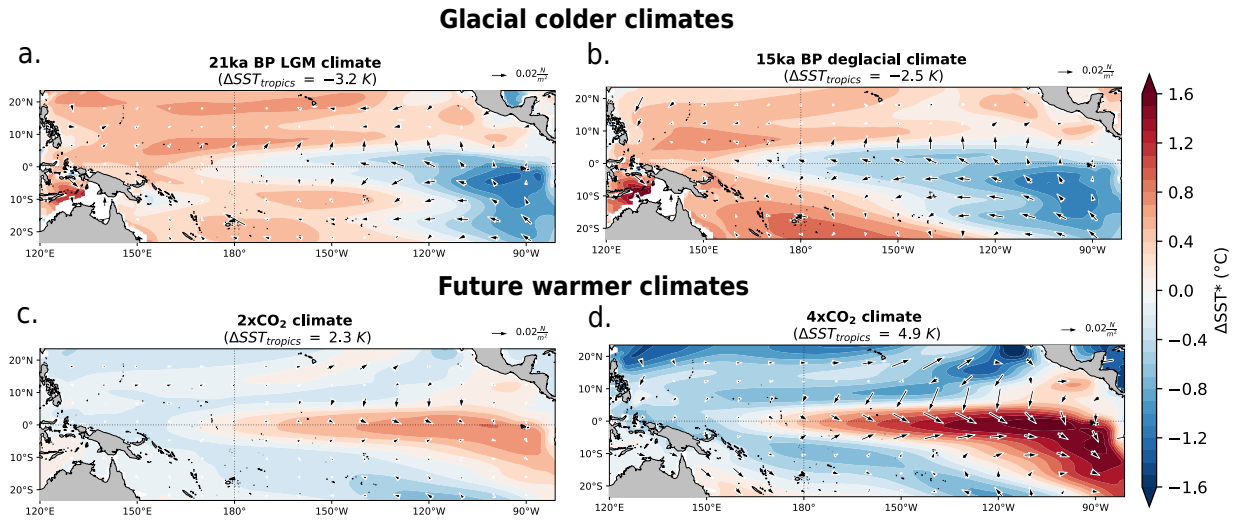

FIG. 1: **Simulated changes in the ocean surface mean state in altered climate states.** Annual mean changes in relative sea-surface temperature (shading), surface wind stress (vectors), and thermocline depth (contours) simulated by the Community Earth System Model Version 1 (CESM1) under altered climatic conditions. Changes for colder climates (top) correspond to equilibrated responses to boundary conditions for glacial intervals 21 and 15 thousand years before present (21ka and 15ka simulations). Changes for warmer climates (bottom) correspond to equilibrated responses to increased greenhouse gas states under doubling and quadrupling of atmospheric CO_2 concentrations ($2xCO_2$ and $4xCO_2$ simulations respectively). Relative SST is defined as the departure from the tropical mean SST (20°N-20°S average) in each climate state. Changes in all variables are computed relative to a simulation of pre-industrial (PI) climate as described in Methods.

mechanism therefore we focus the analysis on the influence of the changes in the mean climate on ENSO dynamics.

Each simulated climate exhibits distinctive patterns of SST and zonal wind stress variability along the equatorial Pacific. In the PI simulation, both SST and wind stress variability feature a single broad maximum in the equatorial central Pacific (Fig. 2b & 3b). By contrast, colder climates display weaker variability in both SST and zonal wind stress, divided into two centers of action – one in the west and one farther east for SST (Fig. 2c-d) and one in the far west and another in the central basin for wind stress (Fig. 3c-d). The dual-center variability pattern seen in glacial climates can be interpreted as a manifestation of both CP and EP ENSO. The western maximum aligns with a westward-shifted CP ENSO, while the eastern maximum indicates a weak EP ENSO (Fig. A4). This analysis confirms that the western Pacific variability is indeed part of the ENSO phenomenon, with its center of action significantly displaced from its modern position. The warmer climates, on the other hand, are characterized by stronger variability in both SST and wind stress extending across the equatorial Pacific, with maximum values in the eastern basin

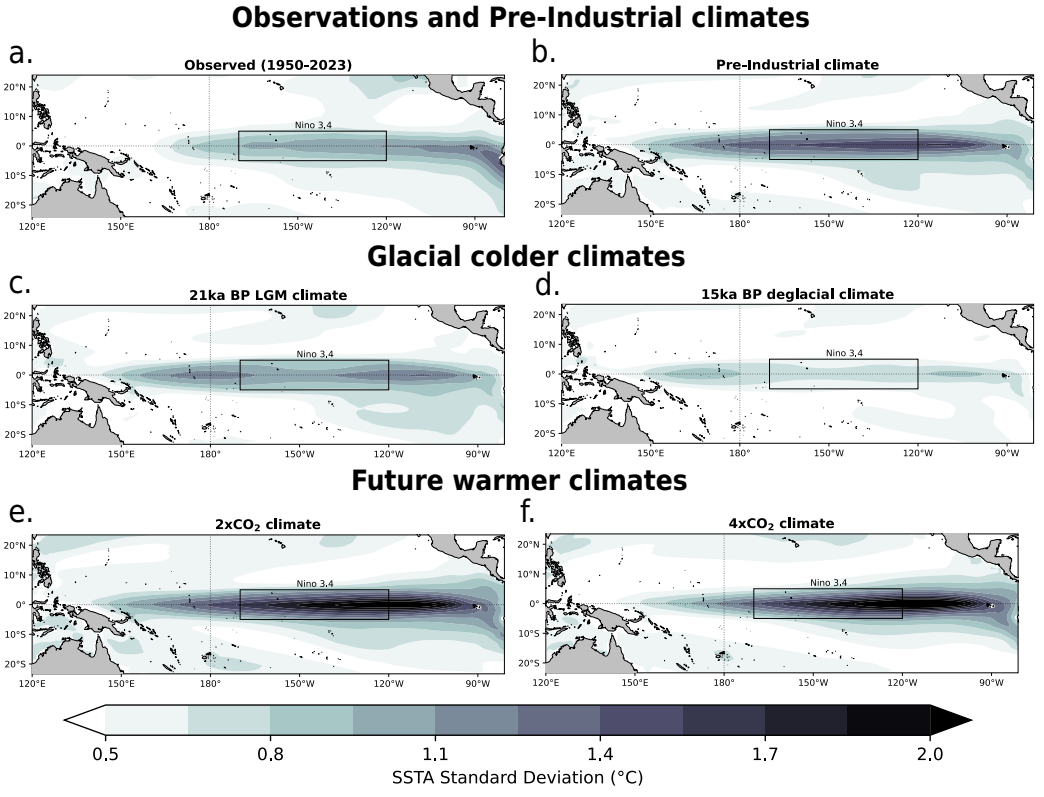

FIG. 2: **Simulated and observed patterns in the anomalous SST variability in altered climate states.** Patterns of anomalous sea-surface temperature (SST) variability (shading) in altered climate states, as simulated by CESM1, compared with observations. Simulated SST variability is calculated as the standard deviation of monthly SST anomalies in each climate state. The fixed location of the Niño3.4 region (170°W–120°W, 5°S–5°N) is highlighted by the black square.

for SST and central basin for wind stress (Fig. 2e-f, Fig. 3e-f). These consistent shifts in SST and wind stress variability across climates are suggestive of zonal shifts in the region of strongest ocean-atmosphere coupling. Locating this area of strong coupling is important to define indices of ENSO variability and to study the physical processes influencing the temporal evolution of events. For instance, if we used the typical Niño-3.4 box for the glacial climates, that region would not fully capture the SST and wind stress variability present in the western equatorial Pacific. Conversely, for the warmer climates the conventional Niño-3.4 definition of coupling region will not capture the SST variability concentrated over the eastern side of the basin.

b. Defining ENSO coupling region for each climate state

Defining an ENSO coupling region in each climate state requires identifying the region where zonal wind stress and SST anomalies are maximally correlated. We achieve this by computing

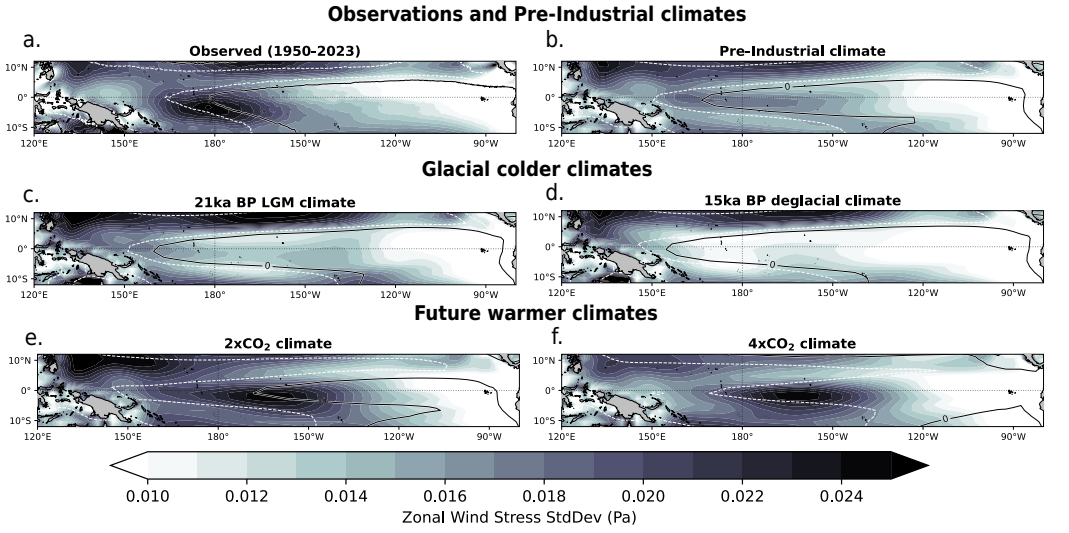

FIG. 3: **Simulated and observed patterns in the anomalous zonal wind stress variability in altered climate states.** Zonal wind stress variability (shading) in altered climate states, as simulated by CESM1. Variability is calculated as the standard deviation of monthly zonal wind stress anomalies in each climate state. The zero contour of vertical velocity at 500 hPa (black solid conour) is shown to indicate the boundary of the western Pacific warm pool in each climate state. One negative interval of vertical velocity is also shown (white dashed contour) to highlight which side of the Pacific corresponds to upward motion.

the leading Empirical Orthogonal Function (EOF1) of zonal wind stress variability across the equatorial Pacific (5°N-5°S, 140°E-80°W). Then we regressed SST anomalies on the normalized principal component (PC1) timeseries of zonal wind stress variability and defined the coupling region of ENSO coupling centered in the location of the maximum SST anomaly regression values. When we apply this approach to observations, the resulting coupling region coincides with the conventional definition based on the Niño3.4 region (Fig. 4a). The PI simulation shows a similar pattern of SST-wind stress co-variability as observed, with the strongest values centered in the Niño3.4 region – although with a stronger SST anomaly amplitude.

Our technique to identify the coupling region reveals pronounced zonal shifts under colder and warmer climates. The most pronounced shift occurs in the deglacial climate (15 ka BP), with a pattern of coupled wind-SST variability displaced westward by 50° of longitude relative to its location in the PI climate (Fig. 4d). The glacial simulation (21 ka BP LGM) shows a less pronounced westward shift of 30° in longitude (Fig. 4c). The $4xCO_2$ simulation shows the most pronounced eastward displacement, with a peak in the pattern of coupled variability shifted 20° to the east of its location in the PI simulation (Fig. 4f), while the $2xCO_2$ simulation shows a comparable eastward shift of 15° (Fig. 4e). These shifts in the location of wind-SST co-variability

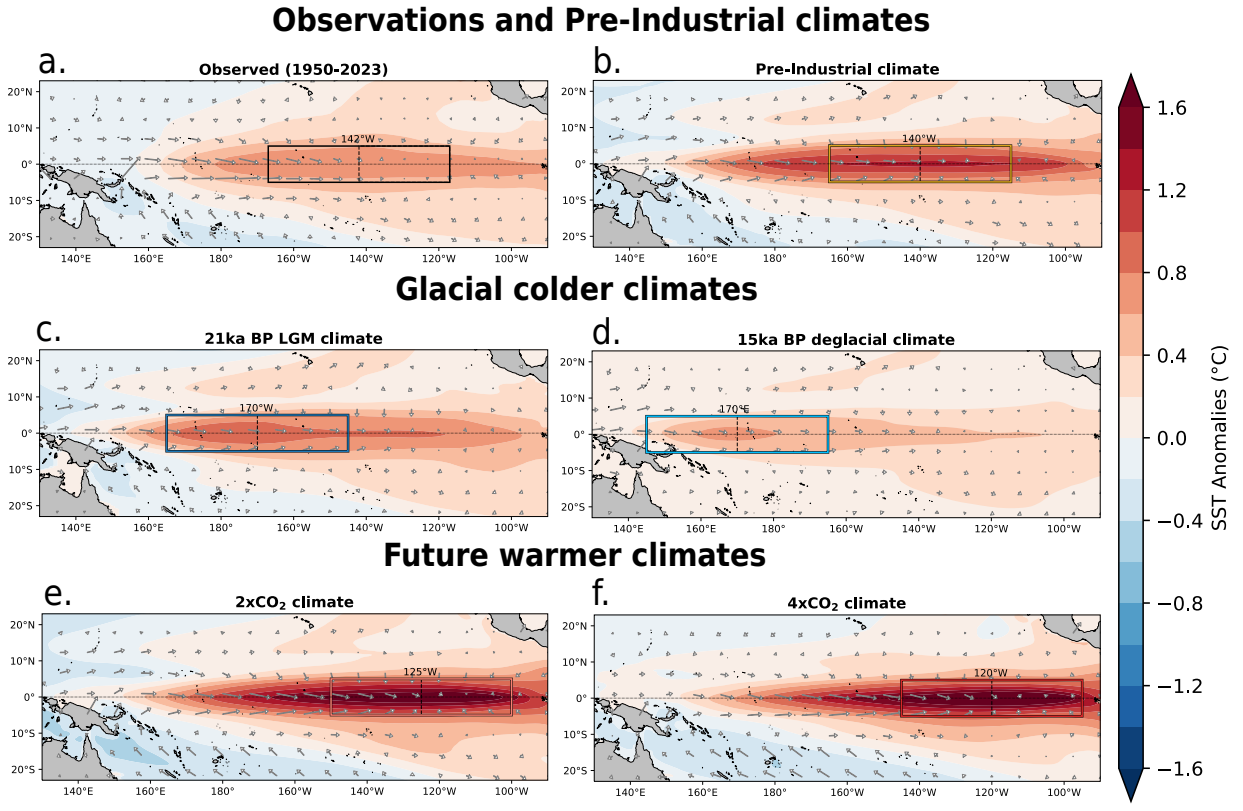

FIG. 4: **Simulated and observed patterns of covariability between SST and zonal wind stress anomalies to identify the ENSO air-sea coupling region.** Patterns of covariability between SST and zonal wind stress anomalies (shading), as simulated by CESM1 and compared with observations, to identify the ENSO air-sea coupling region. Patterns are derived by regressing SST anomalies onto the first normalized principal component of equatorial zonal wind stress variability (5°S–5°N). The vectors represent the regression values of zonal (τ_x) and meridional (τ_y) wind stress onto τ_x PC1. The coupling region is defined as the area extending 25° east and west of the longitude of maximum equatorial SST regression values (box).

align closely with the locations of SST variability maxima depicted in Fig. 2. In colder climates, the westward-shifted region of strong wind-SST coupling correspond only to the location of the western Pacific maxima (Fig. 2c-d), while it is not yet clear why the eastern Pacific maxima is not captured. Despite this, our subsequent analysis of the eastern Pacific demonstrates that it also undergoes significant changes in its oscillatory behavior across different climates (Fig. A1). Similarly, in warmer climates, the eastward-shifted region of strong wind-SST coupling is consistent with the strong SST variability concentrated in the eastern equatorial Pacific (Fig. 2e-f). This highlights the effectiveness of using EOF analysis to accurately capture the zonal shifts in ENSO coupling across our different climate states.

We quantify ENSO SST variability using the CSN index defined based on the coupling region in each climate state (see Methods, Definition of ENSO events). We define the coupling region

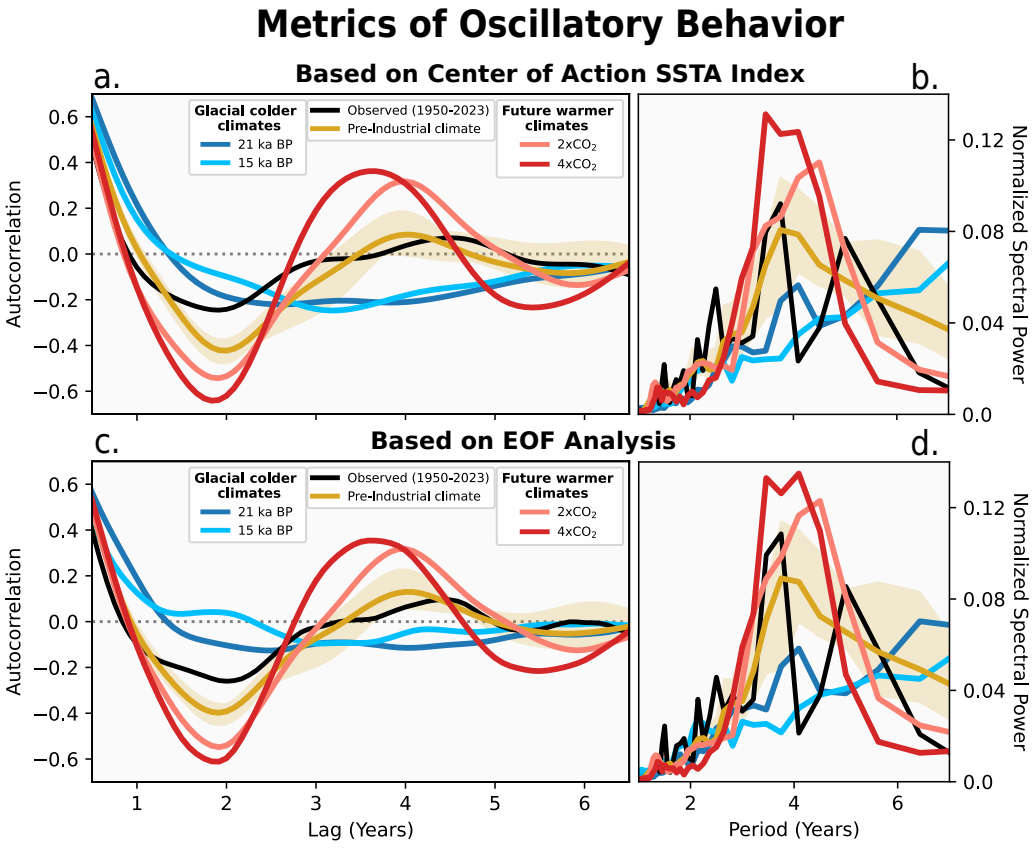

FIG. 5: **Metrics of oscillatory behavior of simulated and observed ENSO variability.** Metrics of oscillatory behavior in observed and simulated ENSO variability across climate states. (a) Lagged autocorrelation of SST anomalies averaged over the ENSO coupling region. (b) Normalized power spectra of SST anomalies averaged over the Climate-Specific coupling region. (c) Same as (a), but for the first principal component (PC1) of SST anomalies across the tropical Pacific (5°S–5°N, 120°E-80°W). (d) Same as (b), but for PC1 of SST anomalies used in (c).

in each climate state spanning 25° of longitude to the east and west of the location of maximal wind-SST co-variability identified before and 5°S-5°N in latitude (Table 2). Defining the Climate Specific Niño (CSN) SST index based on this region ensures that we capture SST variations in the region of maximum coupled variability in each climatic state. To examine how the temporal evolution and frequency characteristics of ENSO variability vary across different climate states, we compute the auto-correlation function (ACF) and the power spectral density (PSD) based on the CSN SST index (Fig. 5). We use the ACF to identify changes in the evolution of ENSO events and the PSD to identify peaks and compare their sharpness across climatic states. We also analyze the ACF and PSD based on PC1 of equatorial SST anomalies to verify that our results are robust to the definition of coupling region.

c. Metrics of oscillatory behavior

The ACF of the CSN index captures the aggregated evolution for both El Niño and La Niña events and should therefore be interpreted with caution, particularly when the evolution of these events is not symmetric as under current climate conditions. Nonetheless, this metric provides useful information on two limits. An ACF that decays to zero correlation without any zero crossing indicates that El Niño and La Niña events are uncorrelated, i.e. that events grow and decay without triggering a subsequent event of the opposite phase. In this case, ENSO would reside in a fully non-oscillatory regime. In contrast, ENSO is fully oscillatory if the ACF shows periodic peaks at a given lag. In this limit, the power spectrum is a delta function at the period of oscillation.

Because the real world ENSO is not a perfect oscillation, the observed lagged ACF shows qualities of both the oscillatory and the damped limits as described above (Fig. 5a & 5c, black curve). The significant negative ACF (-0.2) between 1 to 3 year lags reflects the tendency for El Niño to transition into La Niña events that can last multiple years. The simulated PI climate shows an ACF in striking agreement with observations (Fig. 5a & 5c, yellow curve). The decay of the negative ACF values together with the lack of a positive peak at longer lags reflects the breakdown of oscillatory behavior at the end of La Niña rarely triggering a subsequent El Niño. The absence of positive peaks at multi-year lags indicates that ENSO events lose the memory of past variability after La Niña returns to neutral. This is also reflected in the PSD of observed and PI climate showing a peak at 4 years suggesting a preferred periodicity. However, the broadness of the peak suggests ENSO is not purely oscillatory, just as inferred from the ACF. This is consistent with previous work confirming that CESM1 provides a realistic simulation of ENSO oscillatory dynamics (DiNezio et al. 2017b; Capotondi et al. 2020).

d. Changes in oscillatory behavior

Our simulations show pronounced changes in ENSO oscillatory behavior across the different climatic states. Under glacial conditions, the ACF based on the CSN index and PC1 show a very weak negative correlation at lags longer than one year revealing not just a lack of a transition from El Niño to La Niña, but also a transition to a long-lived, albeit weak, cold state. (Fig. 5a & 5c, blue & light blue curves). This is further reflected by the broader and redder power spectra that shows no significant period consistent with a lack of oscillatory behavior. (Fig. 5b & 5d, blue & light blue

curves). These changes in ACF and PSD in the glacial climates represent a complete breakdown of ENSO oscillatory dynamics. This breakdown is a basin-wide feature, as a lagged autocorrelation analysis for a fixed eastern Pacific region encompassing the secondary activity peak (Figure 2c and 2d), also shows a pronounced lack of oscillatory behavior in colder climates, in contrast to the strong oscillatory signal it shows in warmer climates, underscoring that climate-driven changes in ENSO dynamics are basin-wide (Fig. A1). Conversely, under greenhouse warming, the ACF, either based on the CSN index or the PC1, show a pronounced negative peak at about 2 years, followed by a weaker positive peak at lags between 3.5 and 4 years. These changes are consistent with: 1) a more consistent transition from El Niño to La Niña, and 2) the activation of a La Niña to El Niño transition (Fig. 5a & 5c, orange & red curves). The positive peak in ACF at multi-year lags indicates that the ENSO system retains significant memory of the previous states consistent with increasingly oscillatory behavior in the 2xCO2 and 4xCO2 climates. This is supported by the sharper peaks in the power spectra centered at 3.5 year periodicities (Fig. 5b & 5d, orange and red curves).

Another approach to exploring changes in ENSO oscillatory behavior is through the use of composites of ENSO events. The composite evolution of El Niño and La Niña events for each climate state, constructed using the CSN index as described in the methods section, illustrates these changes (Fig. 6). Unlike the ACF presented previously, these composites separately capture the temporal evolution and actual amplitudes of El Niño and La Niña phases. This separation provides a clearer understanding of the strength and progression of individual ENSO events across each climate. Additionally, the inclusion of probability density functions (PDFs) at key ENSO phases, reveals the distribution of individual events contributing to the composite mean. These PDFs indicate whether most events lean towards neutral, warm, or cold states during the transition period, revealing any changes in the oscillatory dynamics of ENSO in each climate state.

The composite analysis reveals significant differences in ENSO amplitude and transitions across climate states. Under glacial conditions, both El Niño and La Niña events tend to decay into neutral conditions without driving transitions to subsequent phases (Fig. 6a & 6c, blue and light blue curves). In the PI climate, the model realistically simulates El Niño consistently transitioning into La Niña, however, transitions from La Niña to El Niño are infrequent (Fig. 6a & 6c, black and yellow curves). In warmer climates, the transitions from El Niño to La Niña persist as seen in the

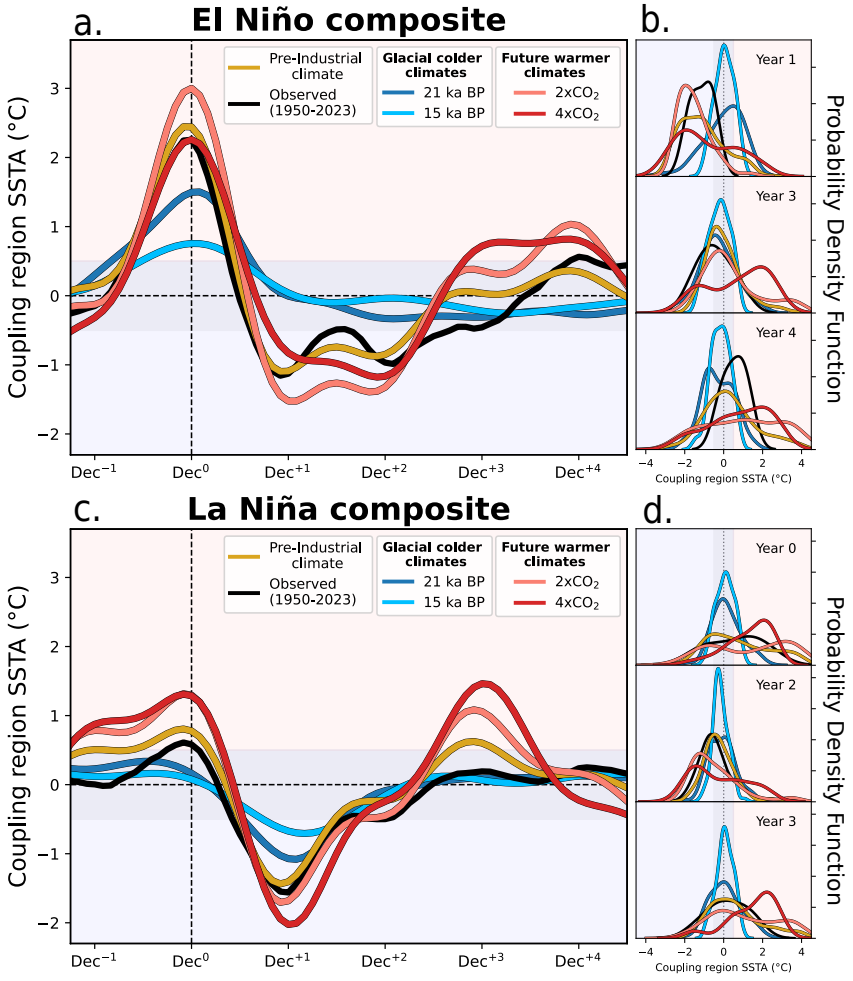

FIG. 6: **Composite evolution of El Niño and La Niña events for the coupling region in each of the altered climate states.** Composite evolution of El Niño and La Niña events based on SST anomalies in the Climate-Specific coupling region, as simulated by CESM1. (a) Composite of El Niño events exceeding a threshold of one standard deviation specific to each climate state, aligned to December, the typical peak month of ENSO in boreal winter. The mean of all events is shown to highlight common behavior, with observations (black solid line) included for comparison with the pre-industrial (PI) simulation. (b) Probability density function showing the distribution of El Niño events at key temporal intervals (years 1, 3, and 4). (c) Same as (a), but for La Niña events. Here the time axis is intentionally shifted by one year relative to the La Niña peak to emphasize the post-peak evolution and transition into subsequent conditions; thus, Dec(+1) corresponds to the peak of La Niña(d) Same as (b), but for La Niña events at key temporal intervals (years 0, 2, and 3) defined relative to this shifted axis.

PI climate, but transitions from La Niña to El Niño become more consistent. This indicates a shift towards a more self-sustained oscillatory behavior in warmer climates (Fig. 6a & 6c, orange and red curves).

e. Mechanisms underlying the changes in oscillatory dynamics

The heat budget analysis allows us to diagnose the processes involved in the changes in oscillatory behavior. Consistent with our earlier findings on SST variability, the glacial climates exhibit temperature anomalies, [T'], with smaller amplitudes (Fig. 7a, blue curve) compared to the PI climate, while warmer climates show temperature anomalies of comparable amplitude (Fig. 7b-c, blue curve). These magnitudes closely align with the rate of temperature change represented by the anomalous temperature tendency, $\frac{\partial[T']}{\partial t}$. For all climates, the evolution of $\frac{\partial[T']}{\partial t}$ (Fig. 7a-c, black curve) is primarily explained by the anomalous thermal advection terms (Fig. 7a-c, brown curve). Ocean advection dominates the heat budget in the glacial and PI climates, where the anomalous net air-sea heat flux contributes negligibly (Fig. 7a-b, yellow curve). In the $4xCO_2$ simulation, however, air-sea heat flux becomes much more active and contributes significantly to the total tendency (Fig. 7c, yellow curve). Note that the anomalous thermal advective terms not included in the calculation of the full heat budget equation are incorporated into the residual term (Fig. 7a-c, magenta line). This residual term is either small in the colder climates or in phase with the total surface layer temperature tendency in the PI and $4xCO_2$ climates. This indicates that any unaccounted physical processes associated with the advective terms, included in the residual term, do not play a significant role in driving ENSO phase transitions. Accordingly, we focus our analysis on the zonal and vertical thermal advection terms, as they are directly in phase with the transition of ENSO events. Notably, the role of anomalous net air-sea heat flux varies across climate states: it is negligible in the glacial and preindustrial climates, where ocean advection alone explains $\frac{\partial[T']}{\partial t}$ (Fig. 7a-b, yellow curve), but becomes significant under $4xCO_2$ forcing (Fig. 7c). In this regime, the flux remains largely in phase with SST anomalies and primarily acts as a damping mechanism, likely contributing to the reduced peak El Niño amplitude relative to the $4xCO_2$ case (Fig. 6a) (Thirumalai et al. 2024), which demonstrates that while advective processes remain the primary drivers of ENSO transitions, the emerging significance of air-sea heat flux in warmer climates serves as the critical moderator of event intensity.

Zonal advection plays a role in driving El Niño events across different climatic conditions, acting as the primary mechanism in PI and glacial climates while becoming less important in the warmer climates. The composites of the anomalous zonal surface current (Fig. 7d-f, purple curve) and its associated anomalous zonal thermal advection (Fig. 7d-f, pink curve), reveal that this process is

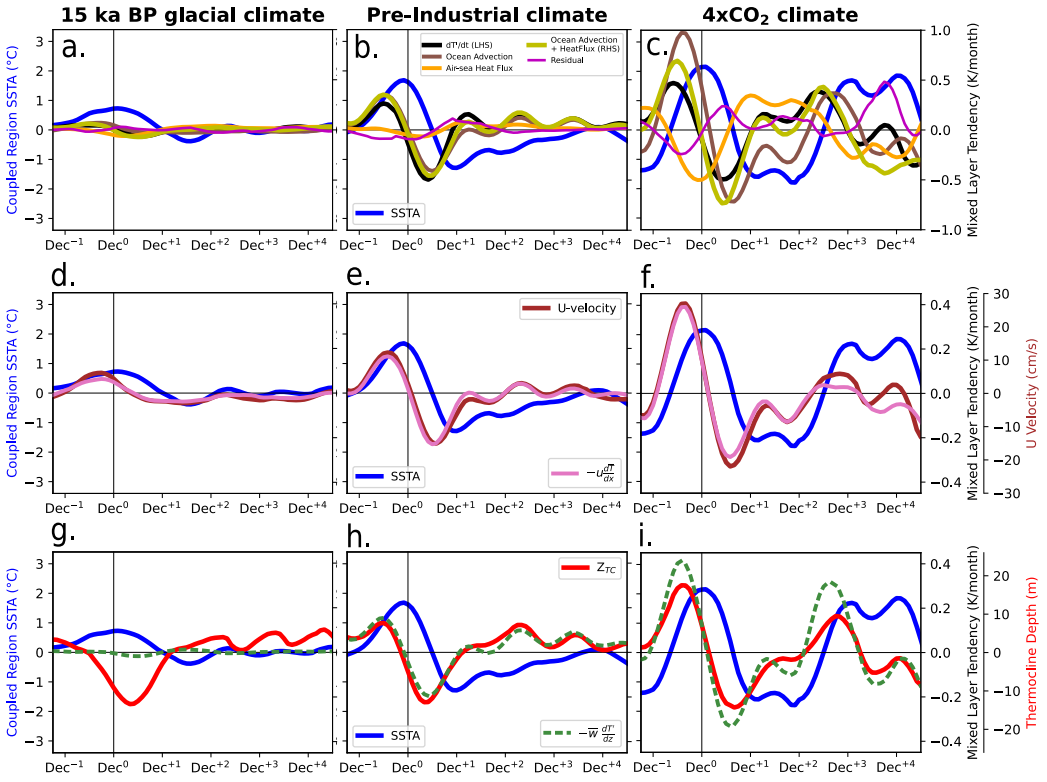

FIG. 7: **Mixed Layer Heat Budget Analysis for each climate state.** Mixed-layer heat budget analysis for El Niño events in each climate state, as simulated by CESM1. Composite heat budget terms are shown during the development, transition, and decay phases of ENSO events, with December of year zero marking the peak of SST anomalies (blue line) in all panels. **Top row**: Heat budget terms include the full tendency (black line), major ocean thermal advection terms (brown line), air-sea heat flux (yellow line), and residual terms (purple line). **Middle row**: Zonal current (dark red line) and its associated zonal thermal advection term (pink line) are displayed. **Bottom row**: The depth of the thermocline (red line) and the vertical thermal advection of anomalous temperature by the mean vertical velocity (green dashed line) are shown, where positive values of the green line indicate a warming tendency and negative values indicate a cooling tendency of the mixed layer. All variables are presented as seasonal anomalies averaged over the Climate-Specific coupling region, defined by equatorial latitudes (5°S-5°N) and longitudes listed in Table 2.

a significant driver of El Niño in the PI climate (Fig. 7e) and serves as the sole driver in glacial climates (Fig. 7d). Despite its crucial role in the PI climate and glacial periods, the anomalous zonal thermal advection does not exhibit significant changes in the warmer climates, particularly during the transition from La Niña to El Niño (Fig. 7f, Dec+2), suggesting a relative stability of this feedback mechanism across different climatic conditions. Therefore, to explore changes across climates, we focus on the anomalous vertical thermal advection term, $-\overline{w}\frac{\partial T'}{\partial z}$, since it is directly linked to thermocline depth variations involved in ENSO event transitions.

Under PI conditions, the location of the coupling region in the central Pacific (170°W-120°W) favors the onset of La Niña after El Niño and hinders the onset of El Niño after La Niña consistent with the evolution of observed events. The composite evolution of ENSO events shows that

the equatorial thermocline shoals after the peak of El Niño (Fig. 7h, red curve), inducing a negative temperature tendency via the anomalous vertical thermal advection, $-\overline{w}\frac{\partial T'}{\partial z}$ (Fig. 7h, green dashed curve). This cooling drives the demise of El Niño and the onset of a subsequent La Niña. Conversely, La Niña is followed by a deepening of the thermocline, producing a positive temperature tendency associated with the anomalous vertical thermal advection. However, this heating is weaker than the cooling that drives the onset of La Niña, making it insufficient to terminate La Niña and trigger a subsequent El Niño as shown by previous work using CCSM4 (DiNezio and Deser 2014), CESM1 (DiNezio et al. 2017b; Wu et al. 2021) and observations (Kessler 2002). This asymmetry in the magnitude of the thermocline-driven thermal advection explains the asymmetric evolution of El Niño and La Niña, consistent with previous work (DiNezio and Deser 2014).

In summary, our heat budget analysis shows that zonal shifts in the coupling region modify how delayed thermocline responses feedback on SSTs, leading to pronounced changes in El Niño and La Niña transitions. Ultimately these shifts explain the different ENSO oscillatory regimes simulated by our model across climatic states. Under glacial conditions, the transition from El Niño to La Niña shows a delayed shoaling of the thermocline, similar to what occurs under PI conditions. However, this anomalously deep thermocline generates a negligible cooling tendency via the anomalous vertical thermal advection (Fig. 7g, green dashed curve). This muted cooling limits the ability of the system to fully transition to a subsequent La Niña. The breakdown of this transition makes El Niño and La Niña grow and decay in isolation, explaining the lack of memory of past ENSO events seen in the ACF and the lack of a clear spectral peak in SST anomalies. In warmer climates, in contrast, the deepening of the thermocline at Dec+3, driven by the peak of La Niña at Dec+2, generates a stronger heating tendency compared to PI conditions (Fig. 7i, green dashed curve). This augmented heating more effectively terminates La Niña and triggers a subsequent El Niño, making ENSO oscillatory.

The simulated changes in thermocline depth, as shown in Figure 8, are consistent with a steady-state response to shifts in the strength of the equatorial trades. The trade winds directly control the east-west tilt of the thermocline—a relationship supported by a zonal momentum balance framework—but they don't determine its overall depth. Instead, the thermocline's depth is constrained at the eastern boundary by the South American coastline's no-normal flow condition,

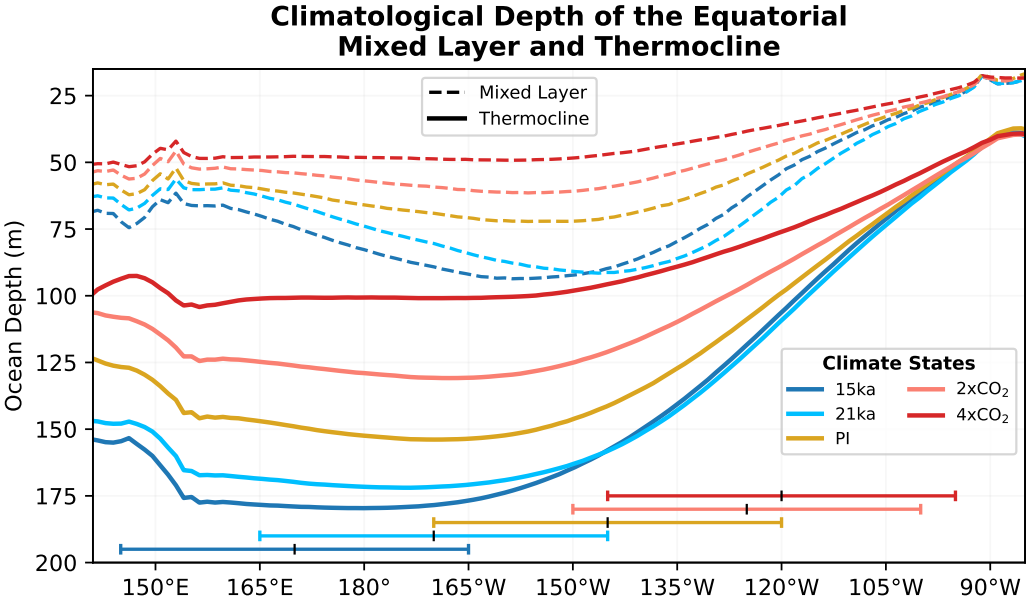

FIG. 8: **Climatological depth of the equatorial mixed layer and thermocline across past and future climate states.** Climatological depth of the equatorial mixed layer (dashed lines) and thermocline (solid lines) across past and future climate states, as simulated by CESM1. Results are shown for the five climate intervals, with horizontal whisker lines at the bottom of the plot indicating the zonal extent of the coupling region for each climate state. The mean depth of both the mixed layer and thermocline shoal in warmer climates and deepens in colder climates, while the relative separation between the thermocline and the mixed layer remains nearly constant across all climates.

which drives upwelling and effectively 'pins' the shallow thermocline in place (Yang and Wang 2009). Consequently, the most significant changes occur in the western and central Pacific, where the thermocline's depth is highly sensitive to the Walker Circulation and its associated wind stress curl (Vecchi and Soden 2007). While our simulations show a deeper thermocline in colder climates and a shallower one in warmer climates, we do not find an intensification (or weakening) of the thermocline-driven anomalous vertical thermal advection, $-\overline{w}\frac{\partial T'}{\partial z}$, across climates when we average the terms of the heat budget over the fixed Niño3.4 region (not shown). This occurs because the deepening of the climatological thermocline in the colder climates is mirrored by a deepening of the climatological mixed layer (Fig. 8, blue curves). Conversely, the shoaling of the climatological thermocline in the warmer climates is mirrored by a shoaling of the climatological mixed layer (Fig. 8, red curves). In both cases the coupling between thermocline and SST variability, i.e. the distance between the thermocline and the base of the mixed layer, remains largely unchanged if we focus on a fixed region across the equatorial Pacific.

In contrast, the main control on ENSO event transitions is the location of the coupling region relative to the depth of the climatological thermocline. In the colder climates, the coupling region is located in the western equatorial Pacific where the climatological thermocline is deep. Conversely, in the warmer climates, the coupling region is located in the eastern equatorial Pacific where the climatological thermocline is shallow (Fig. 8). In the colder climates, thermocline variability produces muted thermal advection into the mixed layer because the thermocline variability during the onset of La Niña produces an anomalous thermal gradient, $\frac{\partial T'}{\partial z}$, located below the climatological mixed layer (Fig. 9b) relative to the PI climate (Fig. 9a). In other words, although the thermocline shoals after El Niño, the associated temperature fluctuations in the thermocline have a muted influence at the base of the mixed layer, explaining the negligible anomalous thermal advection, $-\overline{w}\frac{\partial T'}{\partial z}$, in the heat budget (Fig. 7g). In the warmer climates, thermocline variability during the onset of El Niño produces stronger thermal advection into the mixed layer because the thermocline variability produces an pronounced anomalous thermal gradient, $\frac{\partial T'}{\partial z}$, at the base of the climatological mixed layer (Fig. 9d) relative to the PI (Fig, 9c). In other words, in the warmer climates the coupling region is characterized by a shallower thermocline closer to the base of the mixed layer where thermocline variability can produce stronger anomalous thermal advection, $-\overline{w}\frac{\partial T'}{\partial z}$, as seen in the heat budget (Fig. 7i).

Our analysis shows that delayed thermocline responses are more effective at initiating ENSO events in climate states characterized by a coupling region co-located with a shallow climatological thermocline. Under glacial conditions, the thermocline deepens across the basin and the coupling region shifts westward where the mean thermocline is much deeper. Both effects decouple the thermocline from the surface preventing El Niño to drive a subsequent La Niña. In contrast, under warmer climates, the mean thermocline becomes shallower across the basin and the coupling region shifts eastward where the mean thermocline is much shallower. Both effects make delayed thermocline anomalies more effective at warming the surface during the decay of La Niña, facilitating the transition from La Niña to El Niño. These processes are clearly illustrated in the spatiotemporal evolution of composite events (Fig. 10), which demonstrates that thermocline anomalies can trigger subsequent events when the thermocline-induced SST anomalies occur within the ENSO's specific coupling region for the climate state.

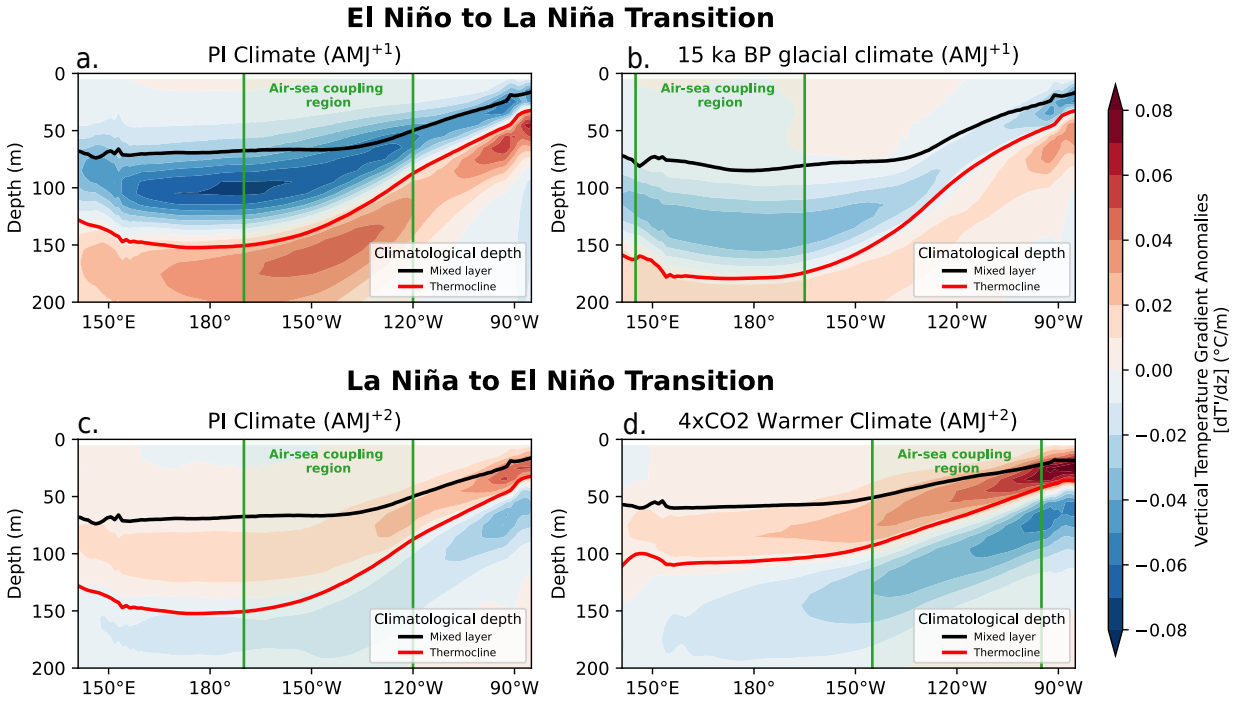

FIG. 9: **Thermocline-mixed layer coupling during the onset of La Niña and El Niño.** Seasonally averaged composites of subsurface vertical temperature gradient anomaly (shading), mixed layer depth (black contour), and thermocline depth (red contour) during phase transitions of ENSO events. Negative (positive) values of vertical temperature gradient (shading) indicate a more (less) thermally stratified upper ocean. (a) Transition from El Niño to La Niña are shown for the April-May-June (AMJ^{+1}) period, 4-6 months after the peak of El Niño for the PI climate. (b) same as (a) but for the 15 ka BP deglacial climate. (c) Transition from La Niña to El Niño are shown for the AMJ^{+2} period, 16-18 months after the peak of La Niña for the PI climate. (b) same as (a) but for the warmer $4xCO_2$ climate.

The spatiotemporal evolution of composite events reveals that delayed thermocline responses generate SST anomalies, which can develop into El Niño or La Niña events depending on whether they occur in regions of strong ocean-atmosphere coupling in each climate state. Under glacial conditions, the shoaling of the thermocline following El Niño cools the ocean surface across much of the equatorial Pacific, driving its termination (Fig. 10a). However, the resulting negative SST anomalies occur too far east of the coupling region. This spatial offset, combined with the weak ocean-atmosphere coupling in that region, prevents the anomalies from amplifying into a subsequent La Niña like in the PI climate (Fig. 10b). In contrast, under warmer conditions, the deepening of the thermocline after the peak of La Niña generates a warming tendency within the coupling region specific to that climate (Fig. 10c). This allows the positive SST anomalies to grow and trigger a subsequent El Niño. These results highlight the critical role of the location of the

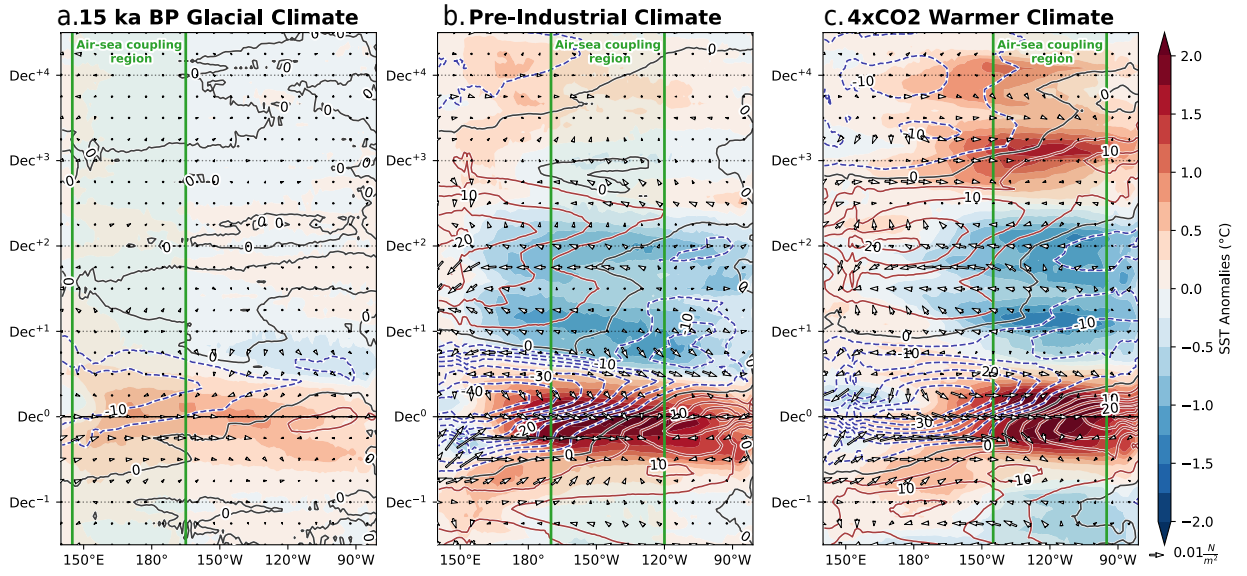

FIG. 10: **Hovmöller plots for El Nino temporal evolution in the 15 ka BP, pre-industrial, and 4xCO2 climates.** Hovmöller plots illustrating the temporal evolution of El Niño events in the 15 ka BP, pre-industrial, and 4xCO_2 climate states, as simulated by CESM1. Longitude–time sections along the equator (5°S–5°N) of SST anomalies (0.25 K intervals, color shading), thermocline depth anomalies (contours, 5 m intervals), and horizontal wind stress anomalies (N m^{-2}, vectors). The analysis focuses on events defined using the Climate-Specific coupling region SST indices for each climate state defined in Table 1.

coupling region in determining the effectiveness of thermocline variations in driving ENSO phase transitions across different climate states.

4. Discussion

Our analysis shows that ENSO oscillatory regimes are controlled by the location of the air-sea coupling region along the equatorial Pacific. Under current and PI conditions this region is located in the central equatorial Pacific coinciding with the Niño-3.4 region. This location hinders the onset of El Niño, driven by delayed thermocline responses associated with a preceding La Niña, explaining one of the more conspicuous asymmetries of the ENSO phenomenon. When the thermocline deepens after La Niña it cannot initiate a subsequent El Niño because the deep climatological thermocline in the central equatorial Pacific limits the magnitude of warming at the ocean surface needed to initiate a subsequent El Niño (DiNezio and Deser 2014). This can be seen in Fig. 10b of our analysis where the thermocline deepening associated with La Niña produces warming in the far eastern equatorial Pacific where the atmosphere is not responsive. The delayed thermocline responses driven by La Niña do not produce warming in the central equatorial Pacific,

where the atmosphere is responsive to SSTs, because the anomalously deep thermocline becomes decoupled from the mixed layer. In contrast, El Niño events can consistently trigger subsequent La Niña because their associated thermocline shoaling can effectively drive cooling in the central Pacific where the atmosphere is response to SSTs. These ideas, originally proposed by DiNezio and Deser (2014), are supported by recent work showing that heat content, a proxy for thermocline depth, is a much better predictor of La Niña than of El Niño (Xue and Kumar 2017; Planton et al. 2018).

Our analysis does not fully explain why the coupling region shifts zonally in response to mean state changes. However, we offer a plausible interpretation based on the results presented here. The eastward expansion of the region of active atmospheric convection, indicated by the eastward shift of the ω_{500} zero contour marking the edge of the western Pacific warm pool in warmer climates (Fig. 3e-f), suggests that enhanced equatorial warming extends the area where the atmosphere is responsive to SST anomalies. This broadening of the convective region would effectively shift the location of strongest wind-SST coupling eastward. Conversely, in colder climates, the westward contraction of the warm pool (Fig. 3c-d) concentrates atmospheric convection and wind-SST coupling further west. We propose this as a hypothesis linking mean state changes to coupling region shifts, rather than a demonstrated mechanism, and identifying the precise drivers of these zonal shifts remains an important direction for future work.

Thermocline variability associated with La Niña can drive subsequent El Niño when the coupling region shifts eastward. In our CESM experiments, greenhouse warming produces enhanced equatorial warming that shifts atmospheric convection and wind responsiveness farther east along the equatorial Pacific (Fig. 3e,f), allowing thermocline variability to play a larger role in the growth of El Niño events. In the PI simulation, by contrast, the colder and drier mean state in the eastern equatorial Pacific limits the atmospheric response to positive SST anomalies, reducing the influence of thermocline-induced warming on El Niño initiation. In our warmer simulations, the eastward shift in the coupling region also increases the effectiveness of thermocline-SST coupling because it occurs over a shallower climatological thermocline (Fig. 8). This shift makes transitions more consistent, contributing to ENSO's transition towards a self-sustained oscillation. This aligns with findings from Cai et al. (2018), who showed a robust increase in EP ENSO SST variability in future greenhouse-warming climates. Conversely, when the coupling region shifts westward,

as in our glacial simulations, the deep climatological thermocline reduces the coupling between thermocline variability and SSTs, preventing the growth of La Niña. In this regime, El Niño and La Niña occur in isolation without influence from previous events via thermocline dynamics. This finding is consistent with paleoclimate records that suggest a weaker ENSO during glacial periods (Thirumalai et al. 2024). As a result of the westward shifted coupling region, the growth of ENSO events is likely to be dominated by stochastic atmospheric variability amplified by the zonal advection feedback at the edge of the warm pool as seen in our heat budget analysis.

Our results are directly relevant to mechanisms proposed to explain changes in the diversity of ENSO spatial patterns ('flavors') under global warming. Greenhouse warming has been argued to flatten the equatorial Pacific thermocline, weakening the thermocline feedback and favoring CP ENSO variability (Yeh et al. 2009), with a flatter thermocline also linked to enhanced CP activity and reduced ENSO amplitude (Lübbecke and McPhaden 2014). Our glacial simulations are broadly consistent with this framework: a deeper mean thermocline and a westward-displaced coupling region weaken thermocline feedbacks and suppress variability. In contrast, our warming experiments reveal a different regime: under $2xCO_2$ and $4xCO_2$ forcing, the thermocline shoals and the coupling region shifts eastward, strengthening—rather than weakening—thermocline feedbacks. This behavior appears inconsistent with the thermocline-flattening mechanism (Yeh et al. 2009), and instead highlights the zonal displacement of the coupling region as a key control on where, and how effectively, the thermocline feedback operates.

This zonal control is consistent with the broader distinction between EP and CP ENSO regimes, which differ in their dominant growth mechanisms: thermocline feedbacks for EP events and zonal advective processes for CP events (Capotondi et al. 2015; Takahashi et al. 2011). Our heat budget analysis supports this interpretation: in warmer climates, an eastward-shifted coupling region enhances thermocline-driven growth consistent with EP-like dynamics, whereas in colder climates, a westward shift favors zonal advection and CP-like behavior. Finally, what we term "oscillatory dynamics" is closely related to ENSO "transitions" (Freund et al. 2024); here, we identify the longitudinal position of the coupling region as a mechanistic control on the regularity of these transitions, rather than treating them solely as an emergent property of ENSO variability.

Our heat budget analysis reveals large changes in the balance of zonal and vertical thermal advection processes during the onset of El Niño. As discussed above, an eastward shift of the

ENSO coupling region makes the delayed thermocline feedback stronger, favoring oscillatory dynamics. However, the eastward shift also strengthens the thermal advection by zonal current anomalies (Fig. 7i) – the main physical process involved in the Bjerknes feedback during the growth of El Niño events (McPhaden and Yu 1999; Thirumalai et al. 2024). We attribute this change to the eastward shift in the coupling region too. The shallower climatological mixed layer over the eastern equatorial Pacific could make zonal currents more responsive to winds allowing a faster expansion of warm pool waters via zonal advective processes. A stronger zonal advection feedback could also favor the onset of El Niño events via stochastic wind variability in addition to a stronger influence from preceding La Niña via thermocline dynamics. This is particularly important for understanding future changes in ENSO variability. Virtually all previous studies of ENSO changes use the the Niño-3.4 region (170°W-120°W) to quantify ENSO variability (e.g., McPhaden et al. 2006; Vecchi and Wittenberg 2010; Timmermann et al. 1999). Our results, particularly the heat budget analysis, suggests that using a fixed region would conflate mechanisms driving changes in amplitude or frequency of ENSO events. We propose that the use of climate specific coupling regions is needed to study the impact of changes in mean climate on all aspects of ENSO variability, not only oscillatory dynamics.

The impact of zonal shifts in the coupling region could also be relevant for understanding ENSO flavors. As El Niño events grow, they are initially driven mostly by zonal advection at the edge of the warm pool where SST anomalies can feedback on the atmosphere McPhaden and Yu (1999). As events grow in magnitude, the atmosphere becomes more responsive to SSTs towards the eastern side of the basin. This shift in the region of coupling can excite the much stronger thermocline feedback in the eastern equatorial Pacific. This is consistent with previous work showing that spatial shifting of the Walker circulation controls ENSO complexity through the increased involvement of processes such as the ocean adjustment to wind stress (Thual and Dewitte 2023) or thermocline feedback (Capotondi 2013).

Although our results are based on a model that simulates a much more realistic ENSO temporal evolution than most other models, CESM1 still simulates too many high-amplitude east Pacific El Niño events. This bias could make ENSO appear more oscillatory, as these events are more prone to transitioning back into El Niño conditions, contrary to what is observed in reality. This does not unduly affect our results given that these events are relatively rare in the PI simulation, as shown by

the realistic behavior of the ACF. However, further research should apply our method to simulations performed with other climate models with realistic ENSO evolution to assess the robustness of our results. Another important aspect to consider is that the altered climates used in our analysis are equilibrated relative to a constant forcing, unlike our current climate which is changing in response to transient forcings that include not only greenhouse gases, but also anthropogenic aerosols, stratospheric ozone change, and other forcing agents. Therefore it is unclear if the projected shift to a fully oscillatory regime will occur under continued emissions of CO_2. Finally, one key feature that requires further investigation is the presence of the two maxima in SST and zonal wind stress variance under glacial conditions (Figs. 2c,d; 3c,d). While the western maximum is linked to the leading mode of variability (PC1), the mechanisms driving the distinct eastern maximum remain unclear. However, we find that this eastern maximum also exhibits a pronounced lack of oscillatory behavior in colder climates, in contrast to the strong oscillatory signal it shows in warmer climates, underscoring that climate-driven changes in ENSO dynamics are basin-wide (Fig. A1). Future studies should focus on understanding this eastern maximum, potentially through targeted model experiments to isolate the underlying physical processes.

CESM, while among the more realistic GCMs in simulating ENSO temporal evolution (DiNezio et al. 2017a; Capotondi et al. 2020), exhibits a known westward bias in the spatial pattern of ENSO SST variability that could in principle affect the sensitivity of the oscillatory behavior identified here. In the PI simulation, maximum SST variability is located near 120°W (Fig. 2b), west of the observed maximum near the South American coast (Fig. 2a), consistent with a westward bias in the mean warm pool edge. This bias is well known in CMIP-class models and is commonly linked to the cold tongue bias. However, our estimate of the coupling region—where ocean-atmosphere feedbacks are most active—is nearly co-located with both the observational estimate and the Nino-3.4 region. This suggests that the bias primarily affects the distribution of variability rather than the location of the key dynamical coupling, and thus is unlikely to fundamentally alter the mechanisms identified here. In the real-world system—where variability is located further east—the coupled system might be closer to a regime of oscillatory behavior, consistent with the idea that ENSO operates near a state of criticality in which modest mean-state changes can alter its dynamical regime (Timmermann et al. 2018).

It is worth distinguishing between two types of model bias. The westward expansion of the warm pool under colder mean states—a bias that directly affects the coupling region where our mechanism operates—is a well-documented feature of CESM and other CMIP-class models. In contrast, the displacement of the SST variability maximum off the South American coast is likely driven by biases in mean SST and weaker coastal upwelling in the eastern Pacific, which affect the manifestation of extreme events rather than the fundamental coupled dynamics. Our analysis focuses on the coupling region, which is less affected by this latter bias.

The modeled response to greenhouse warming—a weakening of the Walker circulation and enhanced equatorial warming (Vecchi and Soden 2007; DiNezio et al. 2009)—has not yet clearly emerged in observations. Instead, recent trends suggest a strengthening of the Walker circulation and zonal SST gradient (Wills et al. 2022). This discrepancy may reflect the influence of internal variability (Heede et al. 2020) or transient responses to external forcings (Heede and Fedorov 2021), which can mask or delay the emergence of the long-term greenhouse response seen in our equilibrated simulations. Paleoclimate evidence from the Pliocene—the most recent interval with CO2 levels comparable to a 2xCO2 climate—supports a weakened zonal SST gradient and Walker circulation (Tierney et al. 2019), consistent with our model's long-term response. However, if greenhouse warming instead produces a strengthening of the zonal SST gradient and equatorial easterly winds—as observed in the glacial climate state simulations—we would expect a westward shift in the coupling region and thus a less oscillatory ENSO.

Despite this uncertainty, our results provide a useful framework for linking changes in the mean state to ENSO predictability. In the 1980s and 1990s, the Pacific experienced a multi-decadal shift toward a weaker Walker circulation and an El Nino-like mean state, during which ENSO was widely considered more predictable than in the recent decades (post year 2000) when the coupled system has shifted toward a stronger Walker circulation and a La Nina-like mean state, more akin to the glacial state in our simulations. Within our framework, these shifts are consistent with changes in the longitudinal position of the coupling region and the resulting modulation of ENSO oscillatory behavior, highlighting the role of the mean state as a key control on predictability.

5. Conclusion

Our simulations demonstrate that El Niño-La Niña transitions and the associated dynamical regimes can experience pronounced changes under altered climatic states. Under global warming, the transition from La Niña to El Niño becomes more consistent, transforming ENSO into a more regular and predictable oscillation. In today's climate, this transition does not happen consistently because the delayed thermocline responses associated with La Niña cannot induce a subsequent El Niño. The thermocline deepening driven by La Niña drives anomalous heating in the central equatorial Pacific, which terminates La Niña; however, as the thermocline deepens, it decouples from the surface, limiting its ability to drive a subsequent El Niño (DiNezio and Deser 2014). This nonlinearity is less pronounced over the eastern equatorial Pacific, where the mean thermocline is sufficiently shallow that it never fully decouples from the surface layer even when it deepens, and thus continues to be effective at influencing SSTs. Yet, this is a region where the atmosphere is not responsive to SST variations because the mean conditions are too cold. However, as the mean climate warms, the atmosphere does become more responsive to SST variability in this eastern Pacific region. The eastward shift in the region of strong coupling produces more regular transitions from La Niña to El Niño because the deepening of the thermocline following La Niña induces SST anomalies in the eastern Pacific that can grow via the Bjerknes feedback. This allows for the termination of La Niña to be followed by a subsequent El Niño, sustaining the ENSO cycle. Conversely, under colder climates, the coupling region of ENSO shifts to the western equatorial Pacific where the climatological thermocline is deep and thus the delayed thermocline shoaling following El Niño cannot produce SST anomalies capable of growing via the Bjerknes feedback. Together these results indicate that ENSO oscillatory behavior is highly sensitive to changes in mean climate, with potential implications for the predictability of El Niño under greenhouse warming.

Acknowledgments. The authors are grateful for the highly constructive comments and suggestions from three anonymous reviewers. Their feedback significantly improved the analysis and clarity of this paper. We also thank Sara Sanchez for their thoughtful feedback and assistance in the revision process. BRM and PDN were supported by grant AGS-2103007. CD was supported by the National Science Foundation - National Center for Atmospheric Research.

Data availability statement. Data underlying this study can be obtained upon request to the corresponding author.

APPENDIX

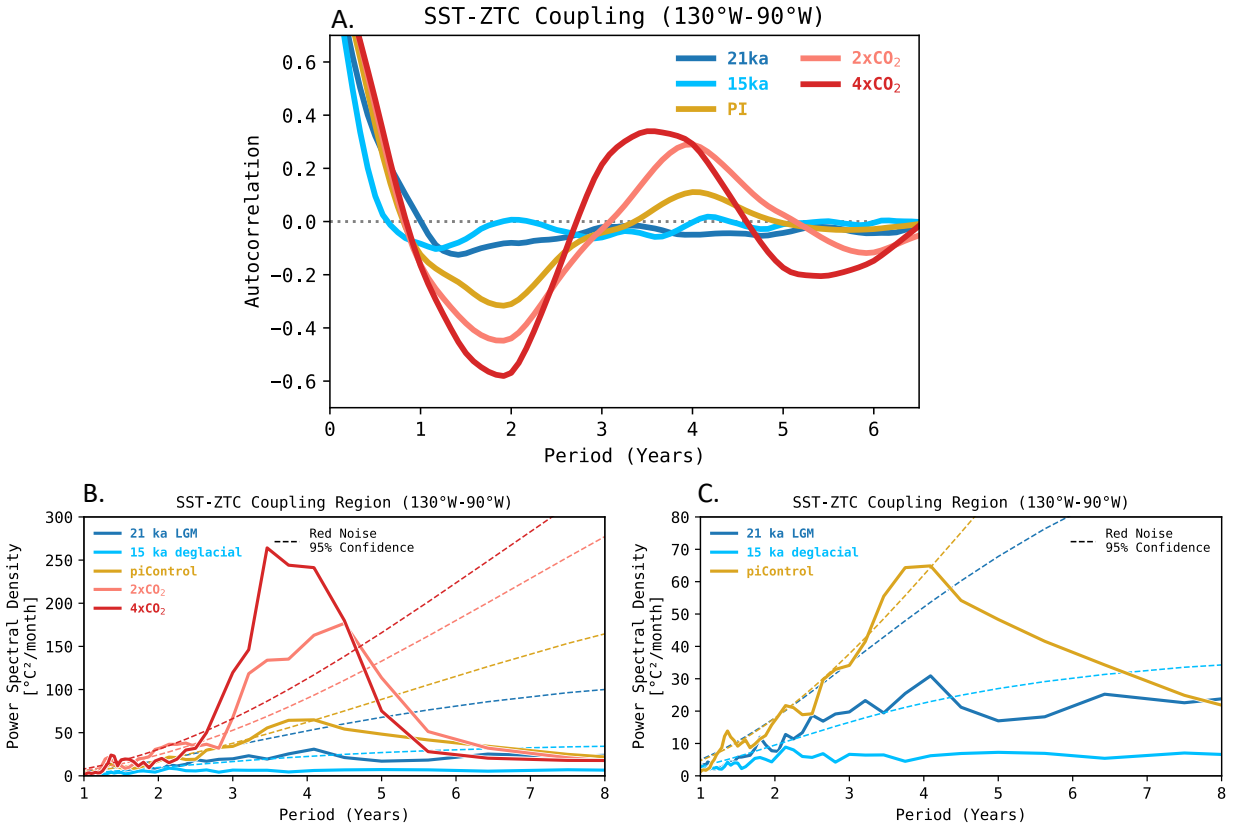

FIG. A1: **SST-ZTC Coupling Region (130°W-90°W) Analysis.** (A) Lagged autocorrelation function of the SST-ZTC index for different climate scenarios (B) Power spectral density of the SST-ZTC index. (C) Same as (B) but power spectral density for just the past climates and pre-industrial (note the smaller y-axis range compared to panel B). The dotted lines in (B) and (C) represent the 95% confidence level using a red-noise spectrum.

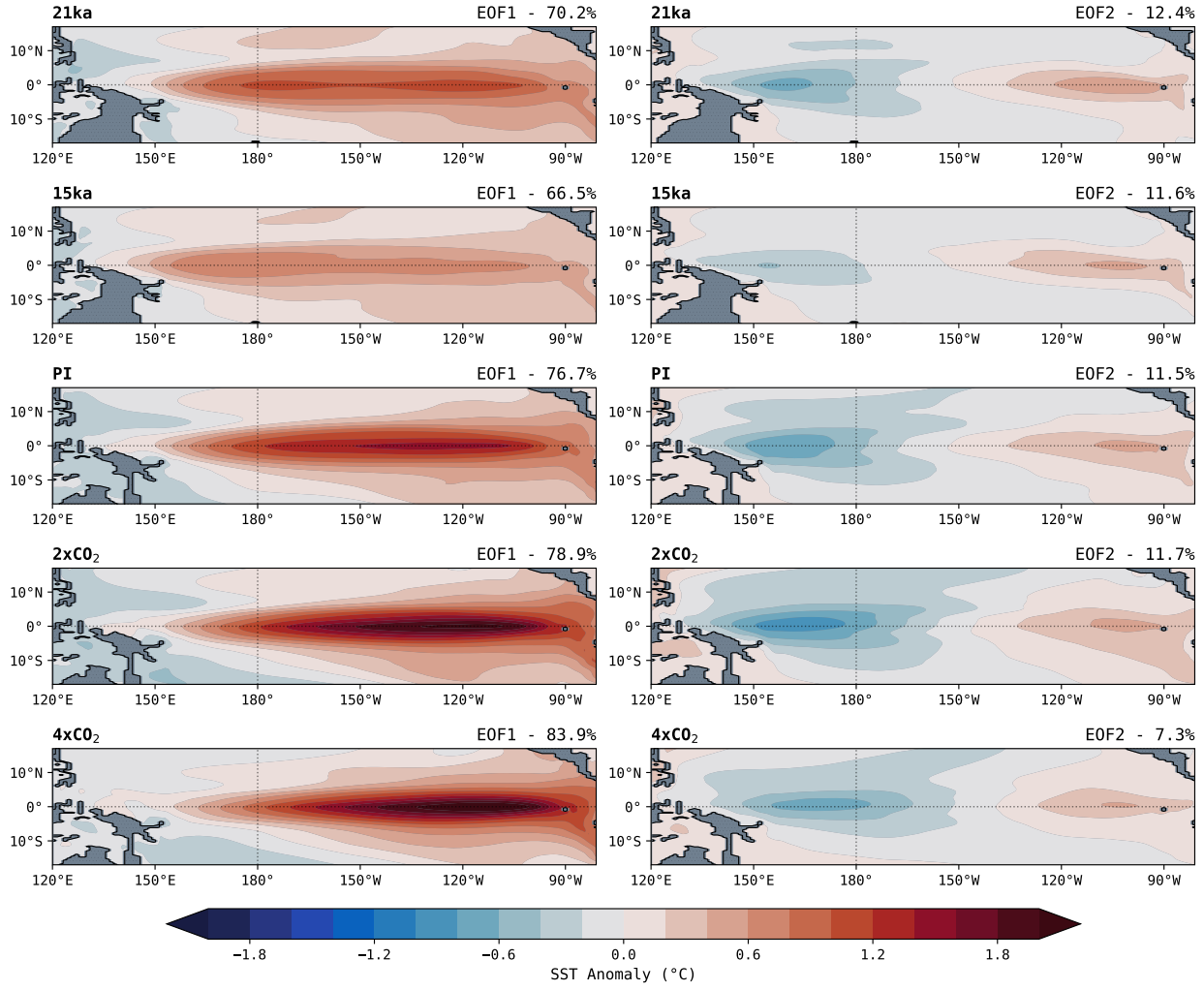

FIG. A2: **Empirical Orthogonal Functions (EOFs) of SST Anomalies.** The left column shows the leading mode pattern of variability for SST anomalies and the right column shows the second mode. The values in the top right corner indicate the percentage of variance explained by each EOF.

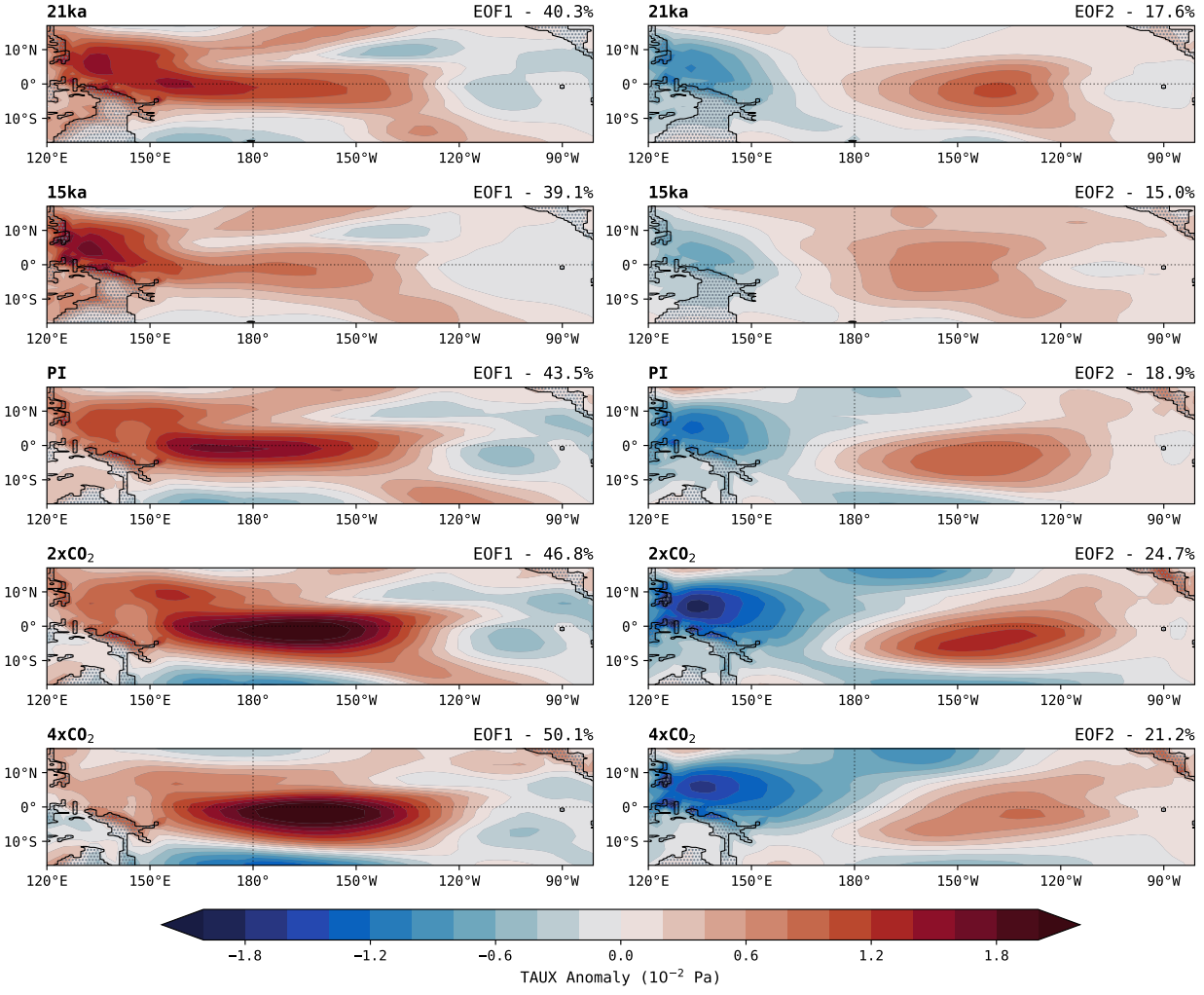

FIG. A3: **Empirical Orthogonal Functions (EOFs) of Zonal Wind Stress Anomalies.** The left column shows the leading mode pattern of variability for zonal wind stress anomalies and the right column shows the second mode. The values in the top right corner indicate the percentage of variance explained by each EOF.

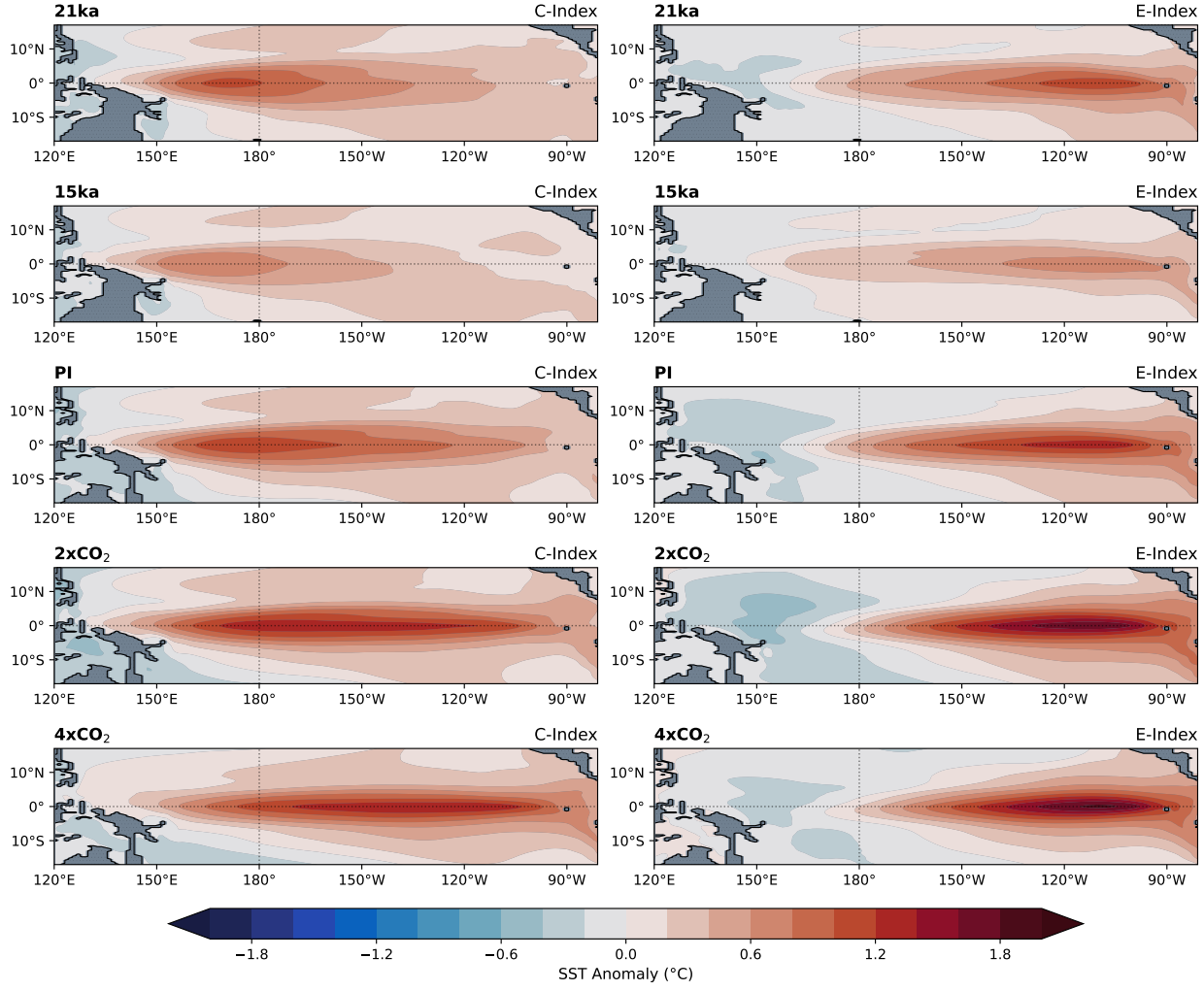

FIG. A4: **Spatial patterns of ENSO indices in different climate scenarios.** The left column shows the Central Pacific (CP) ENSO pattern, calculated using the C-Index, while the right column displays the Eastern Pacific (EP) ENSO pattern, calculated using the E-Index described by Takahashi et al. (2011).

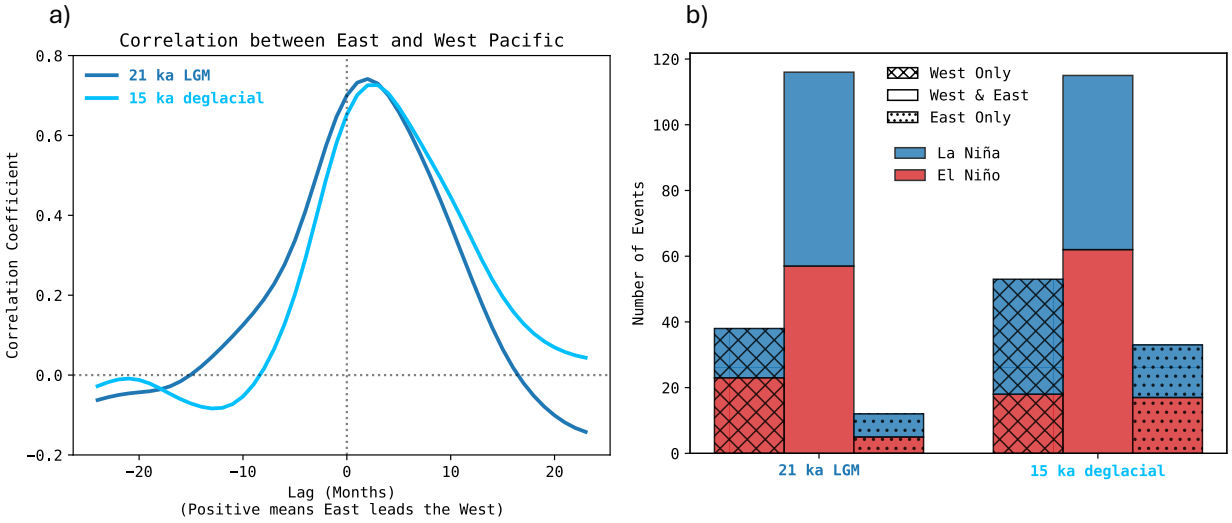

FIG. A5: **Event Characterization in Glacial Climates.** (a) Lagged correlation of equatorial SST anomalies (5°S-5°N) between the western and eastern Pacific. The analysis uses climate-specific western Pacific regions (15ka: 145°E–175°W; 21ka: 160°E–160°W) and a fixed eastern Pacific region (130°W–90°W). (b) Stacked Bar chart showing the number of El Niño and La Niña events in each climate state, categorized into three types: "West Only" events exceed one standard deviation (21ka: 0.9K, 15ka: 0.6K) in the western Pacific while remaining within 0.5 standard deviations in the east. "East Only" events exceed one standard deviation in the eastern Pacific while remaining within 0.5 standard deviations in the west. "West & East" events exceed one standard deviation in both regions simultaneously.

References

Cane, M. A., 2005: The evolution of El Niño, past and future. *Earth and Planetary Science Letters*, **230 (3–4)**, 227–240, https://doi.org/10.1016/j.epsl.2004.12.003.

Capotondi, A., 2013: ENSO diversity in the NCAR CCSM4 climate model. *Journal of Geophysical Research: Oceans*, **118 (10)**, 4755–4770, https://doi.org/10.1002/jgrc.20335.

Capotondi, A., C. Deser, A. S. Phillips, Y. Okumura, and S. M. Larson, 2020: ENSO and Pacific Decadal Variability in the Community Earth System Model Version 2. *J. Advances in Modeling Earth Systems*, **12 (12)**, e2019MS002 022, https://doi.org/10.1029/2019MS002022.

Capotondi, A., and Coauthors, 2015: Understanding ENSO Diversity. *Bull. Amer. Meteor. Soc.*, **96 (6)**, 921–938, https://doi.org/10.1175/BAMS-D-13-00117.1.

Choi, K., G. A. Vecchi, and A. T. Wittenberg, 2013: ENSO Transition, Duration, and Amplitude Asymmetries: Role of the Nonlinear Wind Stress Coupling in a Conceptual Model. *J. Climate*, **26 (23)**, 9462–9476, https://doi.org/10.1175/JCLI-D-13-00045.1.

Clement, A. C., M. A. Cane, and R. Seager, 2001: An Orbitally Driven Tropical Source for Abrupt Climate Change. *Journal of Climate*, **14 (11)**, 2369–2375, https://doi.org/10.1175/1520-0442(2001)014⟨2369:aodtsf⟩2.0.co;2.

Clement, A. C., R. Seager, and M. A. Cane, 1999: Orbital controls on the El Niño/Southern Oscillation and the tropical climate. *Paleoceanography*, **14 (4)**, 441–456, https://doi.org/10.1029/1999PA900013.

De Deckker, P., 2016: The Indo-Pacific Warm Pool: critical to world oceanography and world climate. *Geosci. Lett.*, **3 (20)**, https://doi.org/10.1186/s40562-016-0054-3.

Deser, C., and Coauthors, 2012: ENSO and Pacific Decadal Variability in the Community Climate System Model Version 4. *J. Climate*, **25 (8)**, 2622–2651, https://doi.org/10.1175/JCLI-D-11-00301.1.

DiNezio, P. N., A. Clement, G. A. Vecchi, B. Soden, A. J. Broccoli, B. L. Otto-Bliesner, and P. Braconnot, 2011: The response of the Walker circulation to Last Glacial Maximum forcing:

Implications for detection in proxies. *Paleoceanography*, **26**, PA3217, https://doi.org/10.1029/2010PA002083.

DiNezio, P. N., A. C. Clement, G. A. Vecchi, B. J. Soden, B. P. Kirtman, and S. Lee, 2009: Climate Response of the Equatorial Pacific to Global Warming. *J. of Climate*, **22 (18)**, 4873–4892, https://doi.org/10.1175/2009JCLI2982.1.

DiNezio, P. N., and C. Deser, 2014: Nonlinear Controls on the Persistence of La Niña. *J. Climate*, **27 (19)**, 7335–7355, https://doi.org/10.1175/JCLI-D-14-00033.1.

DiNezio, P. N., C. Deser, A. Karspeck, S. Yeager, Y. Okumura, G. Danabasoglu, and G. A. Meehl, 2017a: A 2 year forecast for a 60–80% chance of La Niña in 2017–2018. *Geophys. Res. Lett.*, **44**, 11,624–11,635, https://doi.org/10.1002/2017GL074904.

DiNezio, P. N., C. Deser, Y. Okumura, and A. Karspeck, 2017b: Predictability of 2-year La Niña events in a coupled general circulation model. *Climate Dyn.*, **49**, 4237–4261, https://doi.org/10.1007/s00382-017-3575-3.

Dommenget, D., T. Bayr, and C. Frauen, 2012: Analysis of the non-linearity in the pattern and time evolution of El Niño-Southern Oscillation. *Climate Dyn.*, **40**, 2825–2847, https://doi.org/10.1007/s00382-012-1475-0.

Freund, M. B., and Coauthors, 2024: Interannual ENSO diversity, transitions, and projected changes in observations and climate models. *Environmental Research Letters*, **19 (11)**, 114 005, https://doi.org/10.1088/1748-9326/ad78db.

Geng, T., F. Jia, W. Cai, L. Wu, B. Gan, Z. Jing, S. Li, and M. J. McPhaden, 2023: Increased occurrences of consecutive La Niña events under global warming. *Nature*, **619 (7971)**, 774–781, https://doi.org/10.1038/s41586-023-06236-9.

Heede, U., and A. Fedorov, 2021: Eastern equatorial Pacific warming delayed by aerosols and thermostat response to CO2 increase. *Nat. Clim. Chang.*, **11**, 696–703, https://doi.org/10.1038/s41558-021-01101-x.

Heede, U. K., A. V. Fedorov, and N. J. Burls, 2020: Timescales and Mechanisms for the Tropical Pacific Response to Global Warming: A Tug of War between the Ocean Thermostat and Weaker Walker. *Journal of Climate*, **33 (14)**, 6101–6118, https://doi.org/10.1175/JCLI-D-19-0690.1.

Hersbach, H., and Coauthors, 2020: The ERA5 global reanalysis. *Q J R Meteorol Soc.*, **146 (730)**, 1999–2049, https://doi.org/10.1002/qj.3803.

Huang, B., and Coauthors, 2017: Extended Reconstructed Sea Surface Temperature, Version 5 (ERSSTv5): Upgrades, Validations, and Intercomparisons. *J. Climate*, **30 (20)**, 8179–8205, https://doi.org/10.1175/JCLI-D-16-0836.1.

Hurrell, J. W., and Coauthors, 2013: The Community Earth System Model: A Framework for Collaborative Research. *Bulletin of the American Meteorological Society*, **94 (9)**, 1339–1360, https://doi.org/10.1175/BAMS-D-12-00121.1.

Jin, F., 1997: An Equatorial Ocean Recharge Paradigm for ENSO. Part I: Conceptual Model. *J. Atmos. Sci.*, **54 (7)**, 811–829, https://doi.org/10.1175/1520-0469(1997)0542.0.CO;2.

Kessler, W. S., 2002: Is ENSO a cycle or a series of events? *Geophys. Res. Lett.*, **29 (23)**, 40–1–40–4, https://doi.org/10.1029/2002GL015924.

Li, G., S. P. Xie, Y. Du, and Y. Luo, 2016: Effects of excessive equatorial cold tongue bias on the projections of tropical Pacific climate change. Part I: The warming pattern in CMIP5 multi-model ensemble. *Climate Dyn.*, **47**, 3817–3831, https://doi.org/10.1007/s00382-016-3043-5.

Liu, Z., Z. Lu, X. Wen, B. L. Otto-Bliesner, A. Timmermann, and K. M. Cobb, 2014: Evolution and forcing mechanisms of El Niño over the past 21,000 years. *Nature*, **515 (7528)**, 550–553, https://doi.org/10.1038/nature13963.

Löfverström, M., and J. M. Lora, 2017: Abrupt regime shifts in the North Atlantic atmospheric circulation over the last deglaciation. *Geophysical Research Letters*, **44 (15)**, 8047–8055, https://doi.org/10.1002/2017gl074274.

Lübbecke, J. F., and M. J. McPhaden, 2014: Assessing the Twenty-First-Century Shift in ENSO Variability in Terms of the Bjerknes Stability Index. *Journal of Climate*, **27 (7)**, 2577–2587, https://doi.org/10.1175/JCLI-D-13-00438.1.

Maher, N., S. B. Power, and J. Marotzke, 2021: More accurate quantification of model-to-model agreement in externally forced climatic responses over the coming century. *Nature Communications*, **12 (1)**, https://doi.org/10.1038/s41467-020-20635-w.

Maher, N., and Coauthors, 2023: The future of the El Niño–Southern Oscillation: using large ensembles to illuminate time-varying responses and inter-model differences. *Earth System Dynamics*, **14 (2)**, 413–431, https://doi.org/10.5194/esd-14-413-2023.

McPhaden, M. J., and X. Yu, 1999: Equatorial waves and the 1997–98 El Niño. *Geophys. Res. Lett.*, **26 (19)**, 2961–2964, https://doi.org/10.1029/1999GL004901.

McPhaden, M. J., S. E. Zebiak, and M. H. Glantz, 2006: ENSO as an Integrating Concept in Earth Science. *Science*, **314 (5806)**, 1740–1745, https://doi.org/10.1126/science.1132588.

Okumura, Y. M., and C. Deser, 2010: Asymmetry in the Duration of El Niño and La Niña. *J. Climate*, **23 (21)**, 5826–5843, https://doi.org/10.1175/2010JCLI3592.1.

Okumura, Y. M., M. Ohba, C. Deser, and H. Ueda, 2011: A Proposed Mechanism for the Asymmetric Duration of El Niño and La Niña. *J. Climate*, **24 (15)**, 3822–3829, https://doi.org/10.1175/2011JCLI3999.1.

Picaut, J., M. Ioualalen, C. Menkes, T. Delcroix, and M. J. McPhaden, 1996: Mechanism of the Zonal Displacements of the Pacific Warm Pool: Implications for ENSO. *Science*, **274**, 1486–1489, https://doi.org/10.1126/science.274.5292.1486.

Planton, Y., J. Vialard, E. Guilyardi, M. Lengaigne, and T. Izumo, 2018: Western Pacific oceanic heat content: A better predictor of La Niña than of El Niño. *Geophys. Res. Lett.*, **45**, 9824–9833, https://doi.org/10.1029/2018GL079341.

Seager, R., M. Cane, N. Henderson, D.-E. Lee, R. Abernathey, and H. Zhang, 2019: Strengthening tropical Pacific zonal sea surface temperature gradient consistent with rising greenhouse gases. *Nature Climate Change*, **9 (7)**, 517–522, https://doi.org/10.1038/s41558-019-0505-x.

Seager, R., N. Henderson, M. Cane, H. Zhang, and J. Nakamura, 2021: Atmosphere-Ocean Dynamics of Persistent Cold States of the Tropical Pacific Ocean. *Journal of Climate*, **34 (13)**, 5195–5214, https://doi.org/10.1175/JCLI-D-20-0620.1.

Suarez, M. J., and P. S. Schopf, 1988: A Delayed Action Oscillator for ENSO. *J. Atmos. Sci.*, **45 (21)**, 3283–3287, https://doi.org/10.1175/1520-0469(1988)0452.0.CO;2.

Takahashi, K., A. Montecinos, K. Goubanova, and B. Dewitte, 2011: ENSO regimes: Reinterpreting the canonical and Modoki El Niño. *Geophysical Research Letters*, **38 (10)**, https://doi.org/10.1029/2011gl047364.

Thirumalai, K., P. N. DiNezio, Y. Okumura, J. Partin, Liu, K. Costa, and A. Jacobel, 2024: Future increase in extreme El Niño supported by past glacial changes. *Nature*, **634**, 374–380, https://doi.org/10.1038/s41586-024-07984-y.

Thual, S., and B. Dewitte, 2023: ENSO complexity controlled by zonal shifts in the Walker circulation. *Nature Geoscience*, **16 (4)**, 328–332, https://doi.org/10.1038/s41561-023-01154-x.

Tierney, J. E., A. M. Haywood, R. Feng, T. Bhattacharya, and B. L. Otto-Bliesner, 2019: Pliocene warmth consistent with greenhouse gas forcing. *Geophys. Res. Lett.*, **46**, 9136–9144, https://doi.org/10.1029/2019GL083802.

Timmermann, A., S. I. An, J. S. Kug, and Coauthors, 2018: El Niño-Southern Oscillation Complexity. *Nature*, **559**, 535–545, https://doi.org/10.1038/s41586-018-0252-6.

Timmermann, A., A. Bacher, M. Esch, M. Latif, and E. Roeckner, 1999: Increased El Niño frequency in a climate model forced by future greenhouse warming. *Nature*, 694–697, https://doi.org/10.1038/19505.

Timmermann, A., S. J. Lorenz, S.-I. An, A. Clement, and S.-P. Xie, 2007: The Effect of Orbital Forcing on the Mean Climate and Variability of the Tropical Pacific. *Journal of Climate*, **20 (16)**, 4147 – 4159, https://doi.org/10.1175/JCLI4240.1.

Tudhope, A. W., and Coauthors, 2001: Variability in the El Niño-Southern Oscillation Through a Glacial-Interglacial Cycle. *Science*, **291 (5508)**, 1511–1517, https://doi.org/10.1126/science.1057969.

Vecchi, G. A., and B. J. Soden, 2007: Global Warming and the Weakening of the Tropical Circulation. *J. Climate*, **20 (17)**, 4316–4340, https://doi.org/10.1175/JCLI4258.1.

Vecchi, G. A., B. J. Soden, A. T. Wittenberg, I. M. Held, A. Leetmaa, and M. J. Harrison, 2006: Weakening of tropical Pacific atmospheric circulation due to anthropogenic forcing. *Nature*, **441 (7089)**, 73–76, https://doi.org/10.1038/nature04744.

Vecchi, G. A., and A. T. Wittenberg, 2010: El niño and our future climate: where do we stand? *WIREs Climate Change*, **1 (2)**, 260–270, https://doi.org/10.1002/wcc.33.

Wang, B., and Coauthors, 2023: Understanding the recent increase in multiyear La Niñas. *Nature Climate Change*, **13 (10)**, 1075–1081, https://doi.org/10.1038/s41558-023-01801-6.

Wills, R. C. J., Y. Dong, C. Proistosecu, K. C. Armour, and D. S. Battisti, 2022: Systematic climate model biases in the large-scale patterns of recent sea-surface temperature and sea-level pressure change. *Geophys. Res. Lett.*, **49 (17)**, e2022GL100 011, https://doi.org/10.1029/2022GL100011.

Wittenberg, A. T., 2009: Are historical records sufficient to constrain ENSO simulations? *Geophys. Res. Lett.*, **36 (12)**, https://doi.org/10.1029/2009GL038710.

Wu, X., Y. M. Okumura, C. Deser, and P. N. DiNezio, 2021: Two-Year Dynamical Predictions of ENSO Event Duration during 1954–2015. *J. Climate*, **34 (10)**, 4069–4087, https://doi.org/10.1175/JCLI-D-20-0619.1.

Xue, Y., and A. Kumar, 2017: Evolution of the 2015/16 El Niño and historical perspective since 1979. *Sci. China Earth Sci.*, **60 (9)**, 1572–1588, https://doi.org/10.1007/s11430-016-0106-9.

Yang, H., and F. Wang, 2009: Revisiting the Thermocline Depth in the Equatorial Pacific. *J. Climate*, **22 (13)**, 3856–3863, https://doi.org/10.1175/2009JCLI2836.1.

Yeh, S. W., B. Dewitte, B. Y. Yim, and Y. Noh, 2010: Role of the upper ocean structure in the response of ENSO-like SST variability to global warming. *Climate Dyn.*, **35**, 355–369, https://doi.org/10.1007/s00382-010-0849-4.

Yeh, S.-W., J.-S. Kug, B. Dewitte, M. Kwon, B. P. Kirtman, and F.-F. Jin, 2009: El Niño in a changing climate. *Nature*, **461 (7263)**, 511–514, https://doi.org/10.1038/nature08316.

Zhu, J., and Coauthors, 2017: Reduced ENSO variability at the LGM revealed by an isotope-enabled Earth system model. *Geophysical Research Letters*, **44 (13)**, 6984–6992, https://doi.org/10.1002/2017gl073406.